

Slow-to-Fast Deformation in Mafic Fault Rocks on an Active Low-Angle Normal Fault, Woodlark Rift, SE Papua New Guinea

M. Mizera¹, T. Little², C. Boulton², D. Prior³, E. Watson⁴, J. Biemiller⁵, J. White⁶, Norio Shigematsu⁷

¹Faculty of Geosciences, Utrecht University, Utrecht, The Netherlands.

²School of Geography, Environment and Earth Sciences, Victoria University of Wellington, Wellington, New Zealand.

³Department of Geology, University of Otago, Dunedin, New Zealand.

⁴GNS Science, Lower Hutt, New Zealand.

⁵Institute for Geophysics, Jackson School of Geosciences, University of Texas at Austin, Austin, Texas, USA.

⁶Department of Earth Sciences, University of New Brunswick, Fredericton, Canada.

⁷Research Institute Earthquake and Volcano Geology, Geological Survey of Japan, AIST

Corresponding author: Marcel Mizera (m.mizera@uu.nl)

Key Points:

- Fault rock microstructures reveal slow-to-fast slip on an active detachment fault that dips 15–24° at the Earth's surface
- Pseudotachylites, foliated cataclasites, and ultracataclasites developed in a zone of mixed mode, seismic-to-aseismic slip behavior
- Frictionally weak saponite in fault gouge promotes slip on the most poorly oriented, surficial part (<24°) of the Mai'iu fault.

Abstract

Slip on the active Mai'iu low-angle normal fault in Papua New Guinea that dips 15–24° at the surface has exhumed in its footwall a single, continuous fault surface across a >25 km-wide dome. Derived from a metabasaltic protolith, the fault zone consists of a <3 m-thick zone of gouges and cataclasites that overprint a structurally underlying carapace of extensional mylonites. Detailed microstructural and geochemical data, combined with chlorite-based geothermometry, reveal changing deformation processes and conditions in the Mai'iu fault rocks as they were exhumed. The microstructure of non-plastically deformed actinolite grains inherited from the fine-grained (6–35 μm) basaltic protolith indicate that shearing at depth was controlled by diffusion creep accompanied by grain-boundary sliding of these grains together with chlorite neo-crystallization at $T > 270\text{--}370^\circ\text{C}$. In a foliated cataclasite unit at shallower crustal levels ($T \approx 150\text{--}270^\circ\text{C}$), fluid-assisted mass transfer and metasomatic reactions accommodated aseismic, distributed shearing; pseudotachylites and ultracataclasites in the same unit indicate that such creep was punctuated by episodes of seismic slip—after which creep resumed.

At the shallowest levels ($T < 150^\circ\text{C}$), gouges contain abundant saponite, a frictionally weak mineral that promotes creep on the shallowest-dipping ($\leq 24^\circ$), most poorly oriented part of the Mai'iu fault. Our field, microstructural and geochemical data of freshly exhumed fault rocks support geodetic, seismological, and geomorphic evidence for mixed seismic-to-aseismic slip on this active low-angle normal fault.

1 Introduction

Domal normal faults (or detachments) that today dip $< 30^\circ$ are key structures accommodating lithospheric extension in both the continents and oceans. Bounding metamorphic core complexes (MCCs), such faults typically have slip magnitudes of tens of kilometres, sufficient to exhume mid-crustal mylonitic rocks in their footwall that have been derived from below the brittle-ductile transition (BDT; e.g., Whitney et al., 2013; Platt et al., 2015). The current low dip of these faults ($< 30^\circ$) near the Earth's surface appears at odds with conventional fault mechanical theory: Anderson-Byerlee frictional fault mechanics predict that normal faults should initiate and slip at dips of $60\text{--}75^\circ$ and frictionally lock-up at dips $< 30\text{--}45^\circ$ (e.g., Anderson, 1951; Sibson, 1985; Lister & Davis, 1989; Collettini & Sibson, 2001; Axen, 2004, 2007; Collettini, 2011; Collettini et al., 2019). This expectation is supported by the rarity of moderate-to-large magnitude historic earthquakes attributable to normal faults with dips $< 30^\circ$ (Jackson, 1987; Jackson & White, 1989; Abers et al., 1997; Collettini et al., 2019). Yet, a small number of normal faults are active at low angles (dips $< 30^\circ$) as indicated by continuous global positioning system (GPS) data for active faults (e.g., Hreinsdóttir & Bennett, 2009; Wallace et al., 2014), and by the alignment of microseismic foci near active faults to depths of up to ~ 16 km (e.g., Rigo et al., 1996; Chiaraluce et al., 2007, 2014). This apparent contradiction is known as the low-angle normal fault (LANF) mechanical paradox.

One way to explain slip on a LANF (or other highly misoriented faults) is that the constituent fault rocks acquire a very low frictional resistance as their fabrics and mineralogy evolve in the brittle crust (e.g., Collettini et al., 2009; Smith et al., 2011). Two main hypotheses allowing sliding at low resolved shear stresses have been suggested: (1) fluid overpressure reduces the effective normal stress (Etheridge et al., 1984; Rice, 1992; Sleep & Blanpied, 1992); or (2) weak minerals such as talc, montmorillonite, saponite and other phyllosilicates lower the coefficient of friction to well below “Byerlee” values ($\mu = 0.6\text{--}0.85$; Byerlee, 1978; Collettini et

al., 2009; Collettini, 2011; Richard et al., 2014). At the onset of grain-scale brittle deformation near the BDT, fluid influx may cause alteration reactions in the protolith rock, leading to the formation of new phyllosilicates or other minerals that are weaker than the original reactant phases (reaction softening; e.g., Wintsch et al., 1995; Wintsch & Yeh, 2013). Such metasomatic reactions together with fluid-assisted diffusive mass transfer (e.g., Rutter & Mainprice, 1979; Rutter, 1983) may promote the development of interconnected networks of weak phases that can reduce the long-term frictional strength of the fault rock to sub-“Byerlee” friction values (textural softening; e.g., Jefferies et al., 2006) leading to mixed frictional-viscous behavior (Bos & Spiers, 2002).

Shear zone weakening may also be promoted by grain-size reduction to activate grain-size-sensitive deformation mechanisms (Warren & Hirth, 2006; Herwegh et al., 2011; Kilian et al., 2011; Bercovici & Ricard, 2012; Montési, 2013; Platt, 2015; Viegas et al., 2016; Stenvall et al., 2019). The latter weakening mechanism can be isochemical, without necessarily requiring presence of a fluid (e.g., Stenvall et al., 2019). A third suggested mechanism for low-angle slip involves rotation of the principal stress axes to “non-Andersonian” orientations to allow slip on an otherwise seemingly misoriented fault; such rotations can arise through a local stress refraction across an interface into a weak fault zone layer (Faulkner et al., 2006; Healy, 2008); or as a result of topographic loads, lateral density variations, and/or horizontal or vertical shear tractions caused by lower crustal flow (e.g., Spencer & Chase, 1989; Yin, 1989 and related comments by Buck, 1990; Westaway, 2005).

Deformational processes operating at different crustal levels along detachment faults are not well understood (e.g., Collettini, 2011; Smith et al., 2011). Most active continental LANFs are concealed beneath a cover of upper plate rocks (Rigo et al., 1996; Chiaraluce et al., 2014), while ancient ones have commonly been overprinted and obscured by post-activity tectonic tilting, chemical alteration, and erosion (e.g., Axen & Bartley, 1997; Axen, 2004; Collettini, 2011; Whitney et al., 2013). The Mai’iu fault in SE Papua New Guinea is a rare exception—it is one of the best preserved of only a handful of known continental LANFs on Earth that are demonstrably active today (e.g., Spencer, 2010). Dip slip on this fault at ~10 mm/yr for the past 3–4 Myrs (Wallace et al., 2014; Webber et al., 2018; Österle, 2019) has exhumed a >29 km width of little-eroded fault surface in its footwall. Along—and immediately beneath—this now abandoned fault surface, freshly exhumed microstructures in the metabasaltic footwall are well-preserved and can be sampled (Little et al., 2019; Mizera et al., 2019). Different types of fault rocks locally crosscut one another, and together they record spatiotemporal changes in the deformation mechanisms accommodating slip as the fault transited through the middle to uppermost crust (Little et al., 2019).

The active Mai’iu fault is an ideal natural laboratory in which to study microstructural and geochemical changes across a wide range of crustal levels. Here, we present data from fault rock samples collected from the exhumed Mai’iu fault. Mostly mafic in bulk composition, the samples comprise pre-extensional non-mylonitic schists (protolith), syn-extensional mylonites, foliated cataclasites, ultracataclasites, and gouges. We combine field observations with mineral phase and elemental composition data of the fault rocks, microstructural imaging and analyses (including grain size and crystallographic-preferred orientation), and chlorite-based estimates of paleotemperatures. By documenting changes in the microstructures and mineralogy of these fault rocks, we derive a syn-exhumational progression of deformation mechanisms and strain rates that accompanied slip on the Mai’iu fault at different structural levels. We also identify processes

(such as metasomatic reactions and grain size reduction) that led to both weakening and transient strengthening of the fault rocks. Our aim is to evaluate: (a) deformation mechanisms accommodating slip on a low-angle normal fault in space and time; and (b) metasomatic changes in the exhuming mafic rocks, in particular those that may have enabled slip on the most highly misoriented part of the fault near the Earth's surface.

2 Tectonic and Geologic Setting of the Mai'iu Fault

The active tectonics of SE Papua New Guinea is governed by the rapid and oblique convergence of the Pacific and Australian plates across an intervening mosaic of microplates (Fig. 1A; Tregoning et al., 1998; Wallace et al., 2004, 2014). The Woodlark-Solomon Sea microplate today rotates counterclockwise at 2–2.7°/Myr relative to the Australian plate about a nearby Euler pole (Wallace et al., 2014). In the active eastern Woodlark Basin, this rotation has resulted in north-south seafloor spreading (Wallace et al., 2004; Eilon et al., 2015). Farther west, the spreading center transitions into a zone of active continental rifting—the Woodlark Rift—which is thought to have initiated at 3.6–8.4 Ma (Fig. 1A; Taylor & Huchon, 2002; Wallace et al., 2014; Cairns et al., 2015).

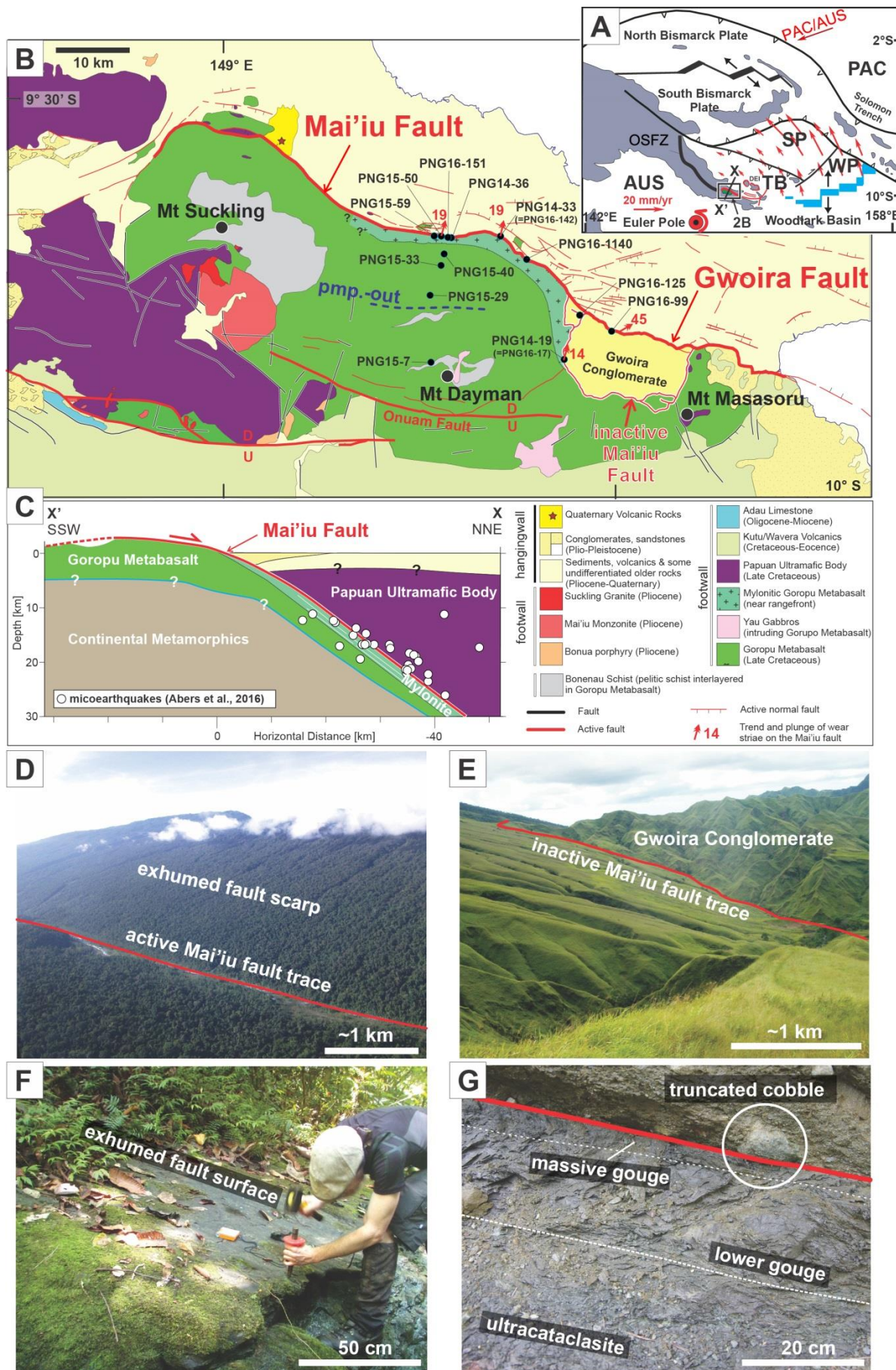


Figure 1. A) Simplified tectonic map of the Woodlark Rift (after Wallace et al., 2004). Locations of Figure 1B and cross-section X-X' of Figure 1C are shown. B) Geological and structural map of the Suckling-Dayman Metamorphic Core Complex (SDM) with sample locations (after Smith & Davies, 1976; Lindley et al., 2014; Little et al., 2019). C) Tectonic cross-section of the Mai'iu fault (after Daczko et al., 2011; Little et al., 2019). Microearthquake foci are based on Abers et al. (2016). D) Oblique aerial photograph of the active Mai'iu fault range front scarp covered in rainforest looking SE. E) Exhumed grassy dip-slopes along the Mai'iu fault where it is inactive and structurally overlain by the Gwoira Conglomerate looking SE. F) Youngest, most recently exhumed surface of the active Mai'iu fault at the base of its scarp. The surface is covered by a dark ~5 cm thick ultracataclasite layer; an overlying soft gouge layer has probably been eroded (site PNG15-50). G) Fault rock sequence of an inactive Mai'iu fault segment preserved beneath the Gwoira Conglomerate (site PNG14-19). Image includes a fault-truncated cobble in the hanging wall (circled). PAC=Pacific plate; AUS=Australian plate; WP=Woodlark plate; SP=Solomon-Sea plate; TB=Trobriand block; DEI=D'Entrecasteaux Islands; OSFZ=Owen-Stanley Fault Zone.

At the southwest margin of the Woodlark Rift (Figs. 1A, 1B), almost all the regional extension is accommodated by slip on the Mai'iu fault. Cosmogenic nuclide studies on the exhumed scarp of this fault indicate a Holocene to present-day dip-slip rate of 11.7 ± 3.5 mm/yr (Webber et al., 2018)—a result that accords with geodetic data indicating a present-day slip-rate of 7.5–9.6 mm/yr (Wallace et al., 2014). The Mai'iu fault is thought to be an extensionally reactivated part of the Owen-Stanley thrust, a major Paleogene thrust fault (Fig. 1A; Davies, 1978; Webb et al., 2008; Daczko et al., 2011; Little et al., 2019). The Owen-Stanley thrust accommodated the southwest-directed obduction of an oceanic and island arc in its upper plate (the Late-Cretaceous Papuan Ultramafic Belt; PUB) over an accreted assemblage of oceanic marginal basin and Australian Plate-derived continental margin rocks (Davies, 1978; Webb et al., 2008; Daczko et al., 2009).

2.1 Geology of the Suckling-Dayman Metamorphic Core Complex

The Mai'iu fault bounds the Suckling-Dayman Metamorphic Core Complex (SDM). The exhumed lower plate of this MCC includes three antiformal culminations that coincide with peaks on the main divide of the Owen Stanley Ranges (Fig. 1B): Mt Suckling (3,576 m), Mt Dayman (2,950 m) and Mt Masasoru (~1,700 m). The footwall of the SDM consists of a >3–4 km thick section of MORB-derived metabasaltic rocks, known as the Goropu Metabasalt, together with minor interbeds of phyllitic metasediments, limestone, and chert, (Smith & Davies, 1976; Österle et al., 2020). The Late Cretaceous metabasalt grades southward into unmetamorphosed equivalents called the Kutu Volcanics, parts of which are Eocene in age (Smith & Davies, 1976). Approximately mid-way up the northern flank of the SDM (Little et al., 2019), a mapped pumpellyite-out isograd probably represents peak temperatures of 350–375°C (Fig. 1B; Beiersdorfer & Day, 1995; Daczko et al., 2009). Farther south, pumpellyite-actinolite facies rocks are exposed as far as the Onuam fault (Fig. 1B), beyond which they transition into prehnite-pumpellyite facies rocks (Davies, 1978) and ultimately the Kutu Volcanics.

Granitoid stocks (e.g., Mai'iu Monzonite, Suckling Granite; Davies & Smith, 1974) intrude the lower plate of the SDM near Mt Suckling and have syn-extensional U-Pb-based zircon crystallisation ages of 1.9–3.7 Ma (Österle et al., 2020). The granitoids record melting of continental crust at depth (Österle et al., 2020). Geophysical surveys (based on seismic travel-times) confirm that the Goropu Metabasalt is underlain by continental crust of felsic to intermediate composition extending to depths of ~32 km near the SDM (Fig. 1C; e.g., Finlayson et al., 1977; Ferris et al., 2006; Eilon et al., 2015; Abers et al., 2016). A relict thrust flap of Papuan Ultramafic Belt (PUB) overlies the Goropu Metabasalt on a southern part of the footwall

of the Mai'iu fault. The PUB is the basement on which the unmetamorphosed alluvial sedimentary rocks of the Gwoira Conglomerate, of Plio-Pleistocene age, were deposited (Fig. 1B; Webber et al., 2020). This latter unit forms much of the hangingwall of the Mai'iu fault, although south of the active Gwoira splay fault, a synformal slice of the Gwoira Conglomerate (former hangingwall rocks) has been captured into the footwall of the SDM (Webber et al., 2020). This slice is floored by a now abandoned, inactive segment of the Mai'iu fault. Outcrops of this inactive segment of the Mai'iu fault provide a complete section through its exhumed fault rocks (Fig. 1B; Little et al., 2019).

Outcrops and dip-slope geomorphic data indicate that the Mai'iu fault dips NNE from 15 to 24° (mostly 20–22°) along its trace at the range front (Figs. 1D, 1F; Little et al., 2019; Mizera et al., 2019). Down-dip of this, a linear alignment of microseismicity indicates that the fault steepens to a 30–40° dip in the subsurface below ~12 km depth (Fig. 1C; Abers et al., 2016). Wear striae on the exposed fault surface, including on fault-truncated cobble facets in the hangingwall, trend ~012–015° (Little et al., 2019). The striae are subparallel to the velocity of the Woodlark-Solomon Sea microplate relative to the Australian Plate farther south (Wallace et al., 2014) (Fig. 1A). The striae trend is also subparallel to numerous megacorrugations in the exhumed footwall of the SDM (Spencer, 2010; Daczko et al., 2011; Little et al., 2019; Mizera et al., 2019).

2.2 Fault rock sequence

The immediate footwall of the Mai'iu fault contains a sequence of mostly mafic-composition fault rocks. Figure 2A shows a schematic section of this sequence, which is partly eroded along the active trace of the fault, but fully preserved in outcrops along the inactive segment of the Mai'iu fault (Fig. 1G). The fault sequence includes five units: a) non-mylonitic schist (protolith); b) mylonite; c) foliated cataclasite; d) ultracataclasite; and e) gouge containing the principal displacement surface. Each unit was briefly described in Little et al. (2019), as summarized below:

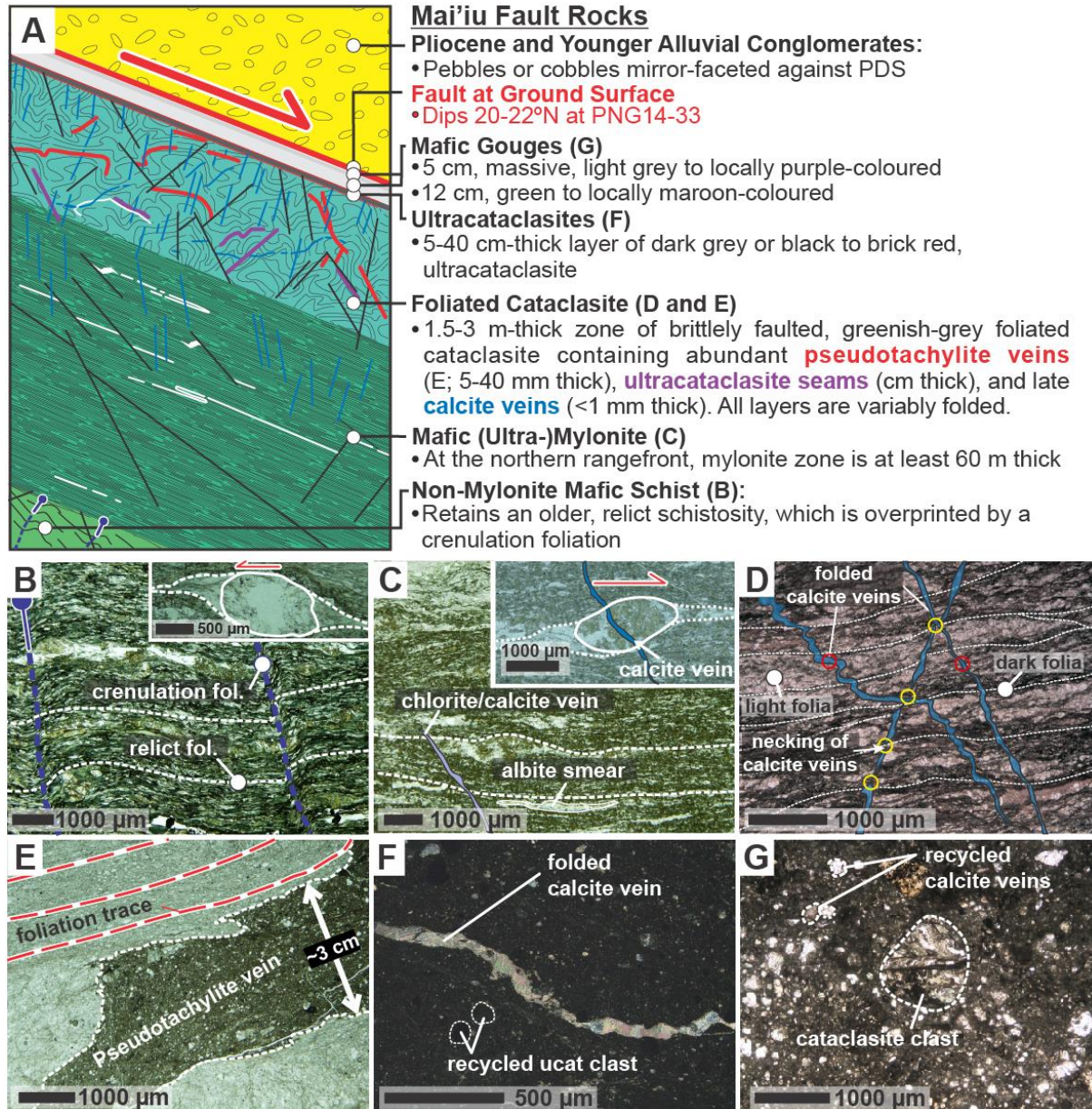


Figure 2. A) Schematic section through the fault rock sequence of the Mai'iu fault based on fully preserved outcrops (modified after Little et al., 2019). B-G) All optical photomicrographs are oriented parallel to the kinematic XZ-direction with down-dip direction to the right. B) Non-mylonitic mafic schist: a spaced crenulation foliation (blue lines) overprints a relict schistosity (white lines; PNG15-7). Inset, asymmetry of strain shadow around epidote porphyroclast indicates top-to-the-SSW shear sense. C) Mafic mylonite: the greenschist facies mineral assemblage defines a LS-tectonite. The rock is cross-cut by several chlorite and calcite veins at a high angle to the foliation. Inset, a strain shadow around an epidote porphyroclast indicates a top-to-the-north (normal) shear sense (PNG14-36). D) Foliated cataclasite: variably deformed calcite veins cross-cut dark and light folia. Note, backward inclined calcite veins (relative to the slip direction) are microfolded (red circles) while forward inclined are necked (yellow circles; PNG16-125B). E) Glassy pseudotachylite vein (~3 cm thick) in a cataclasite sample (PNG14-19). F) Ultracataclasite with folded calcite vein (crossed polarizers; PNG15-50B). Note recycled ultracataclasite (ucat) clasts in the ultrafine-grained matrix. G) Green gouge containing a foliated cataclasite clast and calcite vein fragments (dashed outlines; PNG14-33).

Most of the SDM footwall consists of schistose (non-mylonitic) mafic rocks (Goropu Metabasalt; Fig. 2B) that decrease in metamorphic grade southward (Davies, 1978; Little et al., 2019). On the northern flank of the SDM, greenschist-facies schists contain a fine-grained assemblage of epidote, actinolite, chlorite, albite, titanite, relict clinopyroxene, \pm quartz, \pm calcite, \pm stilpnomelane, \pm pyrite, \pm mica, \pm apatite and \pm opaque minerals (Smith & Davies, 1976; Daczko et al., 2009; Little et al., 2019). The mafic schists have a NNW-trending stretching lineation and a top-to-the-SSW (thrust) sense of shear indicated by: (1) asymmetry of strain fringes filled with fibrous quartz \pm actinolite or of strain shadows around epidote porphyroclasts filled with blocky chlorite (Fig. 2B, inset); (2) extensional (C') shear bands; and (3) the shape-preferred orientation of actinolite porphyroclasts that have fine-grained, sigmoidal tails of chlorite. These shear fabrics developed during the Paleogene Papuan Orogeny when the Goropu Metabasalt was underthrust northward beneath the Papuan Ultramafic Belt along the Owen-Stanley thrust (Little et al., 2019).

Extensional mylonitic fabrics are exposed in the footwall within a ~ 2 km wide band up-dip and to the south of the active fault trace (Fig. 1B). The mylonite unit (mylonites) is at least 60 m-thick along the range front; whereas ~ 2 km up-dip to the south, it narrows to as little as 1.5 m. The mylonites are LS-tectonites with a well-defined NNE-trending stretching lineation and normal-sense shear fabrics (Fig. 2C). Based on pseudosection modelling of the mineral assemblage (epidote, actinolite, chlorite, albite, titanite, \pm quartz, \pm calcite), the mylonites show peak metamorphic conditions of $T=425\pm 50^\circ\text{C}$ and $P=5.9\text{--}7.2$ kbar, reflecting exhumation from $\sim 25\pm 5$ km depth (Daczko et al., 2009).

Above the mylonites, a zone of foliated cataclasite, ultracataclasite, and gouge reaching several metres in thickness overprint and rework the mylonites. The foliated cataclasite unit (foliated cataclasites) is 1.5–3 m-thick and hosts multiple generations of pseudotachylite veins (5–40 mm thick; Figs. 2D, 2E). The pseudotachylite matrices are glassy and amorphous in some of the veins, as verified by quantitative X-ray powder diffraction (see Little et al., 2019). More commonly, however, they are devitrified. Five pseudotachylite veins with glassy matrices were dated by $^{40}\text{Ar}/^{39}\text{Ar}$ geochronology; the derived ages (interpreted as minimum ages for frictional melting) range from 2.24 ± 0.29 Ma to 3.00 ± 0.43 Ma ($\pm 2\sigma$; Little et al., 2019).

The foliated cataclasites are structurally overlain by a 5–40 cm-thick dark grey to black (locally brick-red) ultracataclasite unit (ultracataclasite) (Figs. 1F, 2F). Figure 1F shows the smooth top surface of the ultracataclasite. The fault surface is marked by fine wear striae trending NNE. The ultracataclasite is sharply overlain by a gouge unit (gouge) containing one or more layers of incohesive clay-rich gouge that is preserved in inactive fault segment outcrops beneath the Gwoira Conglomerate (Figs. 1B, 1G, 2G; Little et al., 2019). A sharp, planar slip surface (principal displacement surface) places the unmetamorphosed, hangingwall Gwoira Conglomerate against the gouge (Fig. 1G).

3 Methods

3.1 Thin section preparation and analytical methods

The rock samples were collected in 2014, 2015 and 2016 (Fig. 1B; Little et al., 2019). Thin sections were cut parallel to the kinematic XZ-direction—perpendicular to foliation and parallel to mineral lineation or wear striae on the slip surfaces. Fragile fault rocks (e.g., ultracataclasites and gouges) were impregnated with epoxy resin. The mineralogy,

microstructures, and grain sizes of 157 thin-sections were initially described using optical microscopy. From these, we prepared polished thin sections of 47 representative samples for analysis using a field emission gun scanning electron microscope (FEG-SEM) equipped with energy dispersive spectroscopy (EDS), electron backscatter diffraction (EBSD) detectors, and a cold-cathode cathodoluminescence (CL) microscope at the University of Otago. EDS analyses were used to quantify fault rock elemental compositions (see Supporting Information S1 and S2 for detailed EDS maps and descriptions).

Crystallographic orientation data for the phases actinolite, epidote, titanite, albite and quartz were collected by EBSD. The fabric strength of individual phases in the analysed fault rock samples is given by the misorientation index (M-index)—the stronger the fabric, the greater the M-index, which ranges from 0 (random fabric) to 1 (single crystal; Skemer et al., 2005; Mainprice et al., 2015). Estimated mean grain sizes (diameter of a circle with the equivalent area of a given grain, \bar{D} , with errors given at one standard deviation, $\pm 1\sigma$) are based on EBSD-derived phase maps collected in the kinematic XZ plane (two dimensional). The data were collected with 0.4–2 μm step sizes, and processed using the MTEX toolbox for MATLAB (see Supporting Information S3 to S4 for method description, tables with estimated grain sizes and detailed EBSD phase maps). All fault rock images presented are arranged with the normal slip sense of the Mai'iu fault shown top-to-the-right.

In addition, one fault-truncated cobble from the Gwoira Conglomerate with a mirror-like slip surface was subjected to analysis by transmission electron microscope (TEM) at the University of New Brunswick and by SEM with a HITACHI SU-3500 at the Geological Survey of Japan. A further 12 mylonite and foliated cataclasite samples were subjected to electron probe microanalysis (EPMA) at Victoria University of Wellington. A collection of 15 fault rock samples comprising ultracataclasites and gouges were analysed with X-ray powder diffraction (XRD) at the Centre for Australian Forensic Soil Science (CAFSS), in Urrbrae, South Australia (see also Biemiller et al. submitted). Finally, whole rock major element concentrations of four mafic fault rocks including mylonite and gouge were analyzed using X-ray fluorescence (XRF) at the University of Waikato. All these methods are detailed in the Supporting Information S5 to S9.

3.2 Chlorite-based geothermometry

Chlorite is a common mineral in the Mai'iu fault rocks, where it neocrystallized syntectonically in a range of dilational microstructural sites. Although various empirical geothermometers exploit the relationships between the composition and formation temperature of chlorite (see Bourdelle & Cathelineau, 2015), we employ the geothermometer by Cathelineau (1988) because it is best suited to low-grade metamorphic rocks of basaltic composition (e.g., Bevins et al., 1991). This geothermometer is based on the occupancy of $\text{Al}^{(\text{IV})}$ in tetrahedral sites of the chlorite structure and was calibrated for mafic rocks from 150–300°C using combined microthermometric data, especially fluid inclusion studies on quartz coexisting with clays (Cathelineau & Nieva, 1985; Cathelineau, 1988).

We obtained chlorite compositions with EPMA from six mylonite and six foliated cataclasite samples (296 measurements; Mizera, 2019). The Windows© program WinCcac by Yavuz et al. (2015) was used to calculate the structural formulae of chlorite based on 14 oxygens and to estimate the formation temperatures by applying the geothermometer of Cathelineau (1988). Because chlorite shows considerable variation in structure at low temperatures, including

the possibility of swelling varieties of trioctahedral structure (mixed-layer clays such as smectite-chlorite), we applied the method by W. Wise as presented in Bettison and Schiffman (1988) to calculate the relative fraction of chlorite to “swelling” component (X), where X=1 represents pure chlorite and X=0 represents pure saponite. Bevins et al. (1991) showed that the Cathelineau (1988) thermometer is applicable for $X > 0.55$.

4 Results: Microstructural Observations and Chlorite Geothermometry of the Mai’iu Fault Rock Sequence

4.1 Microstructural and geochemical analyses

4.1.1 Mylonites

Most mafic mylonites contain a well-dispersed, fine-grained mineral assemblage consisting predominantly of epidote ($\varnothing \approx 21 \pm 13 \mu\text{m}$), actinolite ($\varnothing \approx 17 \pm 9 \mu\text{m}$), albite ($\varnothing \approx 18 \pm 11 \mu\text{m}$), titanite ($\varnothing \approx 12 \pm 4 \mu\text{m}$) and chlorite. Porphyroclasts of epidote, actinolite and albite are > 50 – $500 \mu\text{m}$ in diameter. In comparison, the greenschist-facies non-mylonitic schists (protoliths) have similar grain sizes for epidote ($\varnothing \approx 21 \pm 14 \mu\text{m}$), actinolite ($\varnothing \approx 16 \pm 10 \mu\text{m}$), albite ($\varnothing \approx 15 \pm 9 \mu\text{m}$) and titanite ($\varnothing \approx 10 \pm 5 \mu\text{m}$). Unlike the schists, however, the mylonites contain a NNE-trending stretching lineation defined by: a) chlorite strain shadows around epidote porphyroclasts; b) a strong shape-preferred orientation of actinolite and chlorite; and c) smears of albite grains disaggregated from strongly deformed albite-rich veins (Figs. 2C, 3). In addition, the mylonites express a top-to-the-NNE (normal) sense of shear as indicated by extensional C’-shear bands deforming the mylonitic foliation and by the asymmetry of chlorite strain shadows (Fig. 2C, inset). The mylonites are cross-cut by multiple generations of mm-thick chlorite and calcite veins. These are mostly oriented sub-perpendicular to the foliation (Fig. 2C). Less common are mm- to cm-thick veins of albite- and/or quartz that are boudinaged and/or folded within the mylonitic host rock (Figs. 3A, 3D).

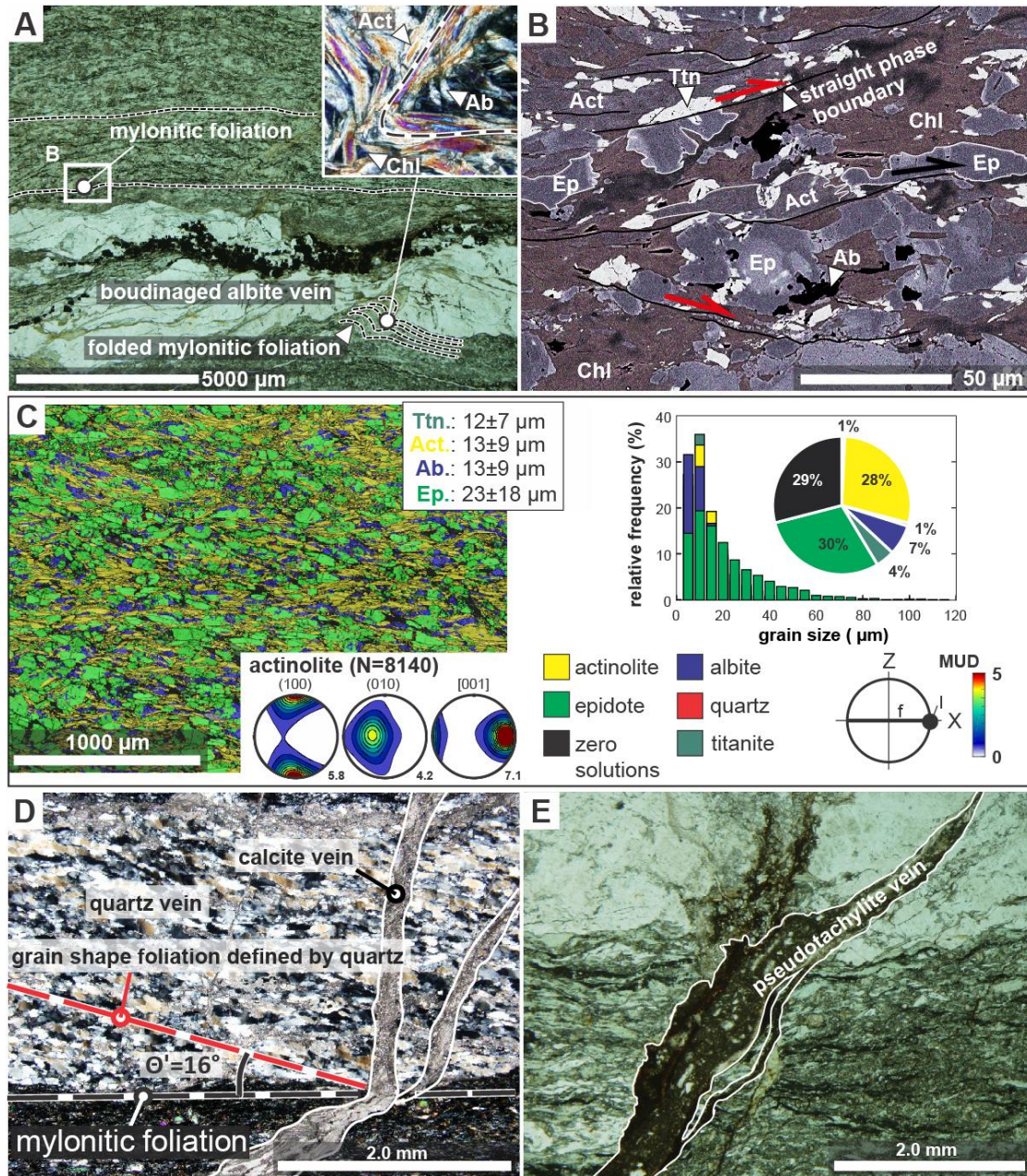


Figure 3. Mafic mylonite samples. A) Optical photomicrograph of a fine-grained mafic mylonite and fragmented boudinaged albite vein (labelled) within the mylonitic host rock (PNG15-59A). Inset, folded mylonitic foliation defined by rotated and fractured actinolite grains. Box denotes area in B. B) Layered elemental image of the mylonite sample in (A) based on EDS analysis. Dark, brick red colors denote chlorite, which we infer to have grown together with the consumption of epidote (purple color) and actinolite (light purple color). Albite grains (black spots) have bulged and irregularly shaped phase boundaries against the other minerals. Thin black lines indicate straight, planar phase boundaries. Grain offsets occur along straight phase boundaries (red arrows). C) Representative EBSD-based phase map, grain-size histogram and phase fraction (%) of mylonite sample PNG16-142C (2 μm step size). Actinolite (100), (010), and [001] pole figures indicate a strong CPO based on one point per grain (N=number of grains). Small numbers next to the pole figures indicate maxima of multiples of uniform distribution (MUD). D) Quartz-rich vein in mylonite PNG16-1BW-E. Elongate quartz grains define a grain-shape foliation oblique ($\sim 16^\circ$) to the mylonitic foliation with a top-to-the-South (thrust) shear sense. E) Optical photomicrograph of a pseudotachylite vein cross-cutting mylonite PNG15-76.

Epidote, actinolite and titanite are subhedral and variably fragmented or microboudinaged (Figs. 3B, 3C). Fractures and microboudin necks in these minerals are filled with chlorite, \pm albite, \pm calcite, \pm quartz, \pm stilpnomelane, and \pm iron oxides. Epidote grains show chemical zonation (based on EDS analysis) where the chemistry changes along the rims of these grains, particularly towards crystal tips and fractures (Fig. 3B; Supporting Information Figure S2.1). Actinolite porphyroclasts are fractured along their long axes, in part displaying fracture-parallel dilational offset in the direction of the mylonitic lineation, and/or at a high-angle to it in areas where the mylonitic foliation contains μm - to mm-scale microfolds (Fig. 3A, inset). Albite and chlorite grains infill the dilational saddle reefs of these folded crystals. The fine-grained fractions (6–35 μm) of epidote, actinolite and titanite have straight phase boundaries against another that are sub-parallel to the mylonitic foliation and that can be traced along several grain widths (Fig. 3B). Epidote, actinolite, and titanite grains have been offset along these straight phase boundaries (Fig. 3B). By contrast, albite grains are commonly irregularly curved or bulged along their phase boundaries with the other mafic minerals. Chlorite grains are intergrown with actinolite and epidote grains (Fig. 3B).

EBSD analyses show that actinolite has a strong crystallographic preferred orientation (CPO) in the mylonites (Fig. 3C) with a mean M-index of 0.2 ± 0.1 (1σ). Lower-hemisphere equal area projections (pole figures; parentheses indicate planes (hkl) and square brackets indicate axes [uvw]) show that the long axes of actinolite grains [001] lie sub-parallel to the stretching lineation and fault-slip direction, whereas poles to (010) and (100) planes concentrate sub-parallel to Y and Z, respectively (Fig. 3C). This CPO is weaker in epidote-rich layers (M-index of ~ 0.09), where fine-grained actinolite grains anastomose around epidote porphyroclasts, and in domains where the mylonitic foliation is microfolded. The strongest actinolite CPOs occur in actinolite-rich layers (M-index of ~ 0.35). Epidote and titanite in mylonitic samples have random to weak CPOs (M-indices of 0.05–0.06). The weak fabrics in these minerals are defined by a tendency for the poles to (010)-planes to be aligned sub-parallel to the slip-direction, and [001]-axes sub-perpendicular to it. Actinolite, epidote and titanite do not show intragranular microstructures indicative of crystal-plastic deformation (e.g., undulose extinction, subgrain boundaries, deformation lamellae, bulging, etc.). Albite has a random to weak CPO in the matrices of all analyzed fault rocks (Supporting Information S4).

Deformed veins of monophase quartz are usually arranged sub-parallel to the mylonitic foliation (Fig. 3D). Elongated quartz grains within these veins define a grain shape fabric that is oblique to the mylonitic foliation ($\sim 16^\circ$) and consistently indicate a top-to-the-south (thrust) sense of shear. In the veins, porphyroclastic quartz grains are surrounded by fine, ~ 5 – $15 \mu\text{m}$ -sized quartz grains similar to a “core and mantle” microstructure. Quartz porphyroclasts in these veins have interlobate and bulged grain boundaries at a wavelength similar to the size of the finer quartz grains, suggesting dynamic recrystallization by bulging (e.g., Stipp et al., 2002; Stipp and Kunze, 2008; see also Little et al., 2019).

Mafic mylonites are locally cross-cut by ~ 0.5 – 1 mm thick seams of ultrafine-grained (optically irresolvable) rock containing fragments of epidote, albite, quartz, titanite, abundant pyrite and mylonite wall-rock clasts. The seams are mostly discordant to the mylonitic foliation and have strongly indented, intrusive contacts indicating injection (Fig. 3E). We interpret these to be pseudotachylite veins similar to the aforementioned ones hosted by the nearby foliated cataclasite unit.

4.1.2 Foliated cataclasites

The contact between the mylonites and foliated cataclasites locally coincides with one or more, mm- to cm-thick, anastomosing bands of ultramylonite. The contact zone is also marked by upward increases in the intensity of microfaulting and brecciation and the degree of apparent bleaching of the metabasaltic protolith. The cataclasites contain a mm- to cm-spaced foliation defined by alternating dark- and light-colored folia (Figs. 2D, 4). Darker, phyllosilicate-rich folia anastomose around light-coloured domains and lenticular clasts that consist of albite-rich material. This spaced foliation is distinct from the much finer and more continuous foliation in the mylonites (Figs. 2C, 2D). The spaced foliation is folded at the mm- to cm-scale and is locally cross-cut by (less folded) pseudotachylite veins and abundant, μm - to <1 mm-thick calcite gash veins (Fig. 4A). The calcite veins are typically oriented sub-perpendicular to the foliation. Backward-inclined gash veins (with respect to the sense of shear) are shortened and folded, while forward-inclined ones are stretched and show necking structures (Fig. 2D)—a change in strain type compatible with a normal-sense shearing of the wall rocks. Locally, bands of ultracataclasite cross-cut the folded mylonitic fabric, the calcite veins embedded within it (Fig. 4B), and the pseudotachylite veins.

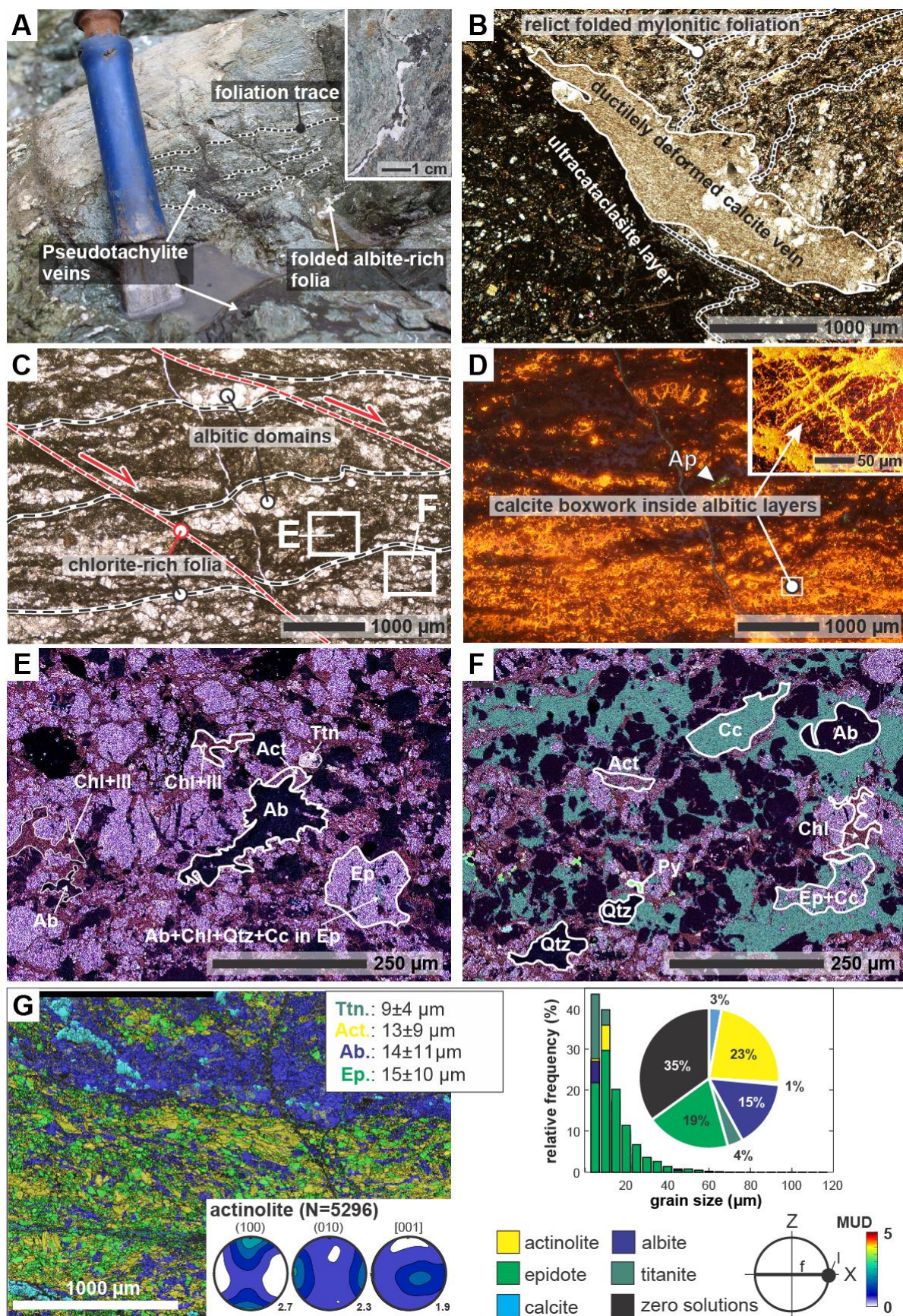
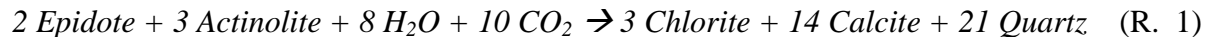


Figure 4. Foliated cataclasite samples. A) Field photograph of a foliated cataclasite cross-cut by several pseudotachylite veins (dark seams; PNG14-19). Dashed lines indicate foliation trace. Inset, folded calcite and pseudotachylite vein. B) Optical photomicrograph (crossed polarizers) of a foliated cataclasite preserving folded ghosts of the mylonitic foliation (upper right) and ductilely deformed calcite vein (center) cross-cut by an ultracataclasite layer (PNG16-50B). C) Optical photomicrograph of foliated cataclasite PNG16-17D2H. Light layers contain albite, calcite and quartz (Fig. 4F); dark folia (black lines) contain predominantly chlorite±illite, plus minor epidote and actinolite (Fig. 4E). Two dark seams consisting of predominantly chlorite (red line) define an S-C' fabric. D) Optical cathodoluminescence of (C) highlights calcite box-work (orange; inset) inside albite layers. E) Layered elemental image of the dark, chlorite-rich folia in (C) created using EDS analyses. Dark, brick red colors indicate chlorite. We infer that chlorite grew and was passively concentrated during a reaction that consumed epidote (purple color) and actinolite (purple-red color). Epidote is highly fractured and filled with albite, quartz, calcite or chlorite. Relict albite and quartz grains (dark grains) have bulged or irregularly shaped grain boundaries against the other phases. F) Layered elemental image of a light-colored layer in (C) created using EDS analyses. This light layer is dominated by calcite (light green grains) and albite (dark grains). Minor amounts of mafic minerals (epidote, actinolite and chlorite) are also present. G) Representative EBSD-based phase map, grain-size histogram and phase fraction (%; pie diagram) of foliated cataclasite sample PNG16-142E (2 µm step size). Pole figures of (100), (010), and [001] indicate that the CPO of actinolite grains, based on one point per grain (N=number of grains), is weaker than in mylonites and oblique to the kinematic axes. Small numbers next to the pole figures indicate maxima of multiples of uniform distribution (MUD).

Most of the dark folia consist of phyllosilicates (<2 µm in size), with lesser epidote (Ø≈17±9 µm), actinolite (Ø≈12±7 µm) and titanite (Ø≈9±4 µm; Figs. 4C, 4E). EDS and XRD analyses indicate that the phyllosilicates are dominated by chlorite and lesser 1Md and 2M1 illites (Supporting Information S1, S2; also Little et al., 2019). Epidote and actinolite grains typically have indented or truncated phase boundaries in contact with chlorite. Bulging of chlorite inwardly into epidote and actinolite grains suggests growth of chlorite together with dissolution and removal of the neighboring phase (Figs. 4C, 4E). Albite, calcite and quartz are rare in the dark-coloured folia. Where preserved in these folia, the albite grains are either (1) anhedral with interlobate or sutured phase boundaries in contact with the other mafic minerals; or (2) preserved as inclusions inside larger epidote grains together with calcite, quartz and/or chlorite inclusions (Fig. 4E). Based on these observations, we propose the following common mineral reaction responsible for the transformation of epidote and actinolite to chlorite in (sub)greenschist-facies metabasalt (Hashimoto, 1972; Skelton et al., 2000, and references therein):



If this fluid-driven metasomatic reaction was operative, we would expect calcite and quartz to be formed at the expense of actinolite and epidote.

Indeed, in the light-colored, mm-thick albitic domains, abundant neorecrystallized calcite and quartz occurs in grain-scale dilation sites (Figs. 4C, 4F). Optical cathodoluminescence microphotographs reveal pervasive micro-veining and cementation of the light domains by calcite (Fig. 4D). Albite grains (Ø≈12±9 µm) are usually anhedral, untwinned and cross-cut by either calcite veins or the dark-coloured folia. EPMA analyses of albite porphyroclasts in the mylonite and of albite in the light-coloured foliated cataclasite layers indicate an average composition of An₀₅ in both settings, but the albite in the foliated cataclasite shows a wider compositional spread (Fig. 5A).

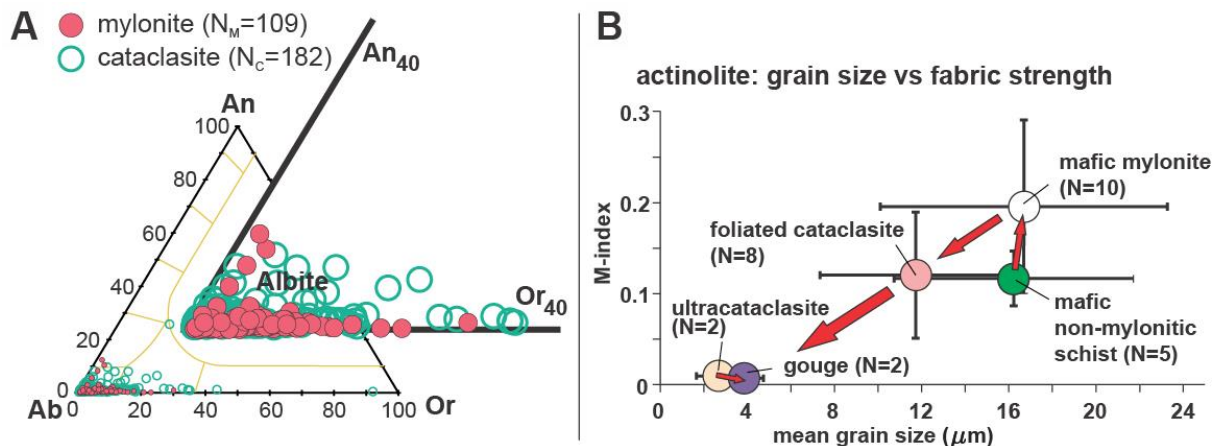


Figure 5. A) Feldspar composition in mafic mylonites and foliated cataclasites. Feldspars are ~95% albite (see also Daczko et al., 2009). B) Grain size vs. M-index plot of actinolite CPOs (averaged values; N=number of samples analysed). The arrowed trend depicts a strong grain-size reduction and weakening of the CPO strength from the mafic mylonites to the foliated cataclasites and ultracataclasites.

Epidote, actinolite and titanite in both the dark and light folia of the foliated cataclasites, show a decrease in grain size, shape preferred orientation and CPO strength relative to the mafic mylonites (Fig. 5B). The average CPO of actinolite in the foliated cataclasites has an M-index of 0.12 ± 0.07 (1σ), compared with an average M-index of 0.2 ± 0.1 (1σ) in the mylonites. While some cataclasite samples have actinolite CPOs similar in strength to mylonites, most are weaker, displaying (010) poles and [001] axes that are diffuse and/or girdled in directions oblique to the kinematic axes (Fig. 4G). Epidote, titanite and albite do not show a CPO in the foliated cataclasites, nor in any of the other overlying fault rocks (M-indices < 0.03).

4.1.3 Ultracataclasites

The ultracataclasites are unfoliated and too fine-grained ($< 2 \mu\text{m}$) to be optically resolved in thin section (Fig. 6A). XRD, EDS and EBSD analyses reveal that mafic grains (epidote, actinolite, titanite and albite; all $\approx 2 \pm 1 \mu\text{m}$), potassium (K-)feldspar, and older (recycled) ultracataclasite lithic fragments are embedded in a much finer-grained ($< 1 \mu\text{m}$), clay-rich matrix (Fig. 6B). Epidote and actinolite porphyroclasts in the ultracataclasite unit are up to $50 \mu\text{m}$ in diameter, fractured, and show ragged boundaries at the contact with the surrounding clay-rich matrix (Fig. 6E). These epidote and actinolite porphyroclasts are likely to have been reworked from the underlying foliated cataclasite (Fig. 6A).

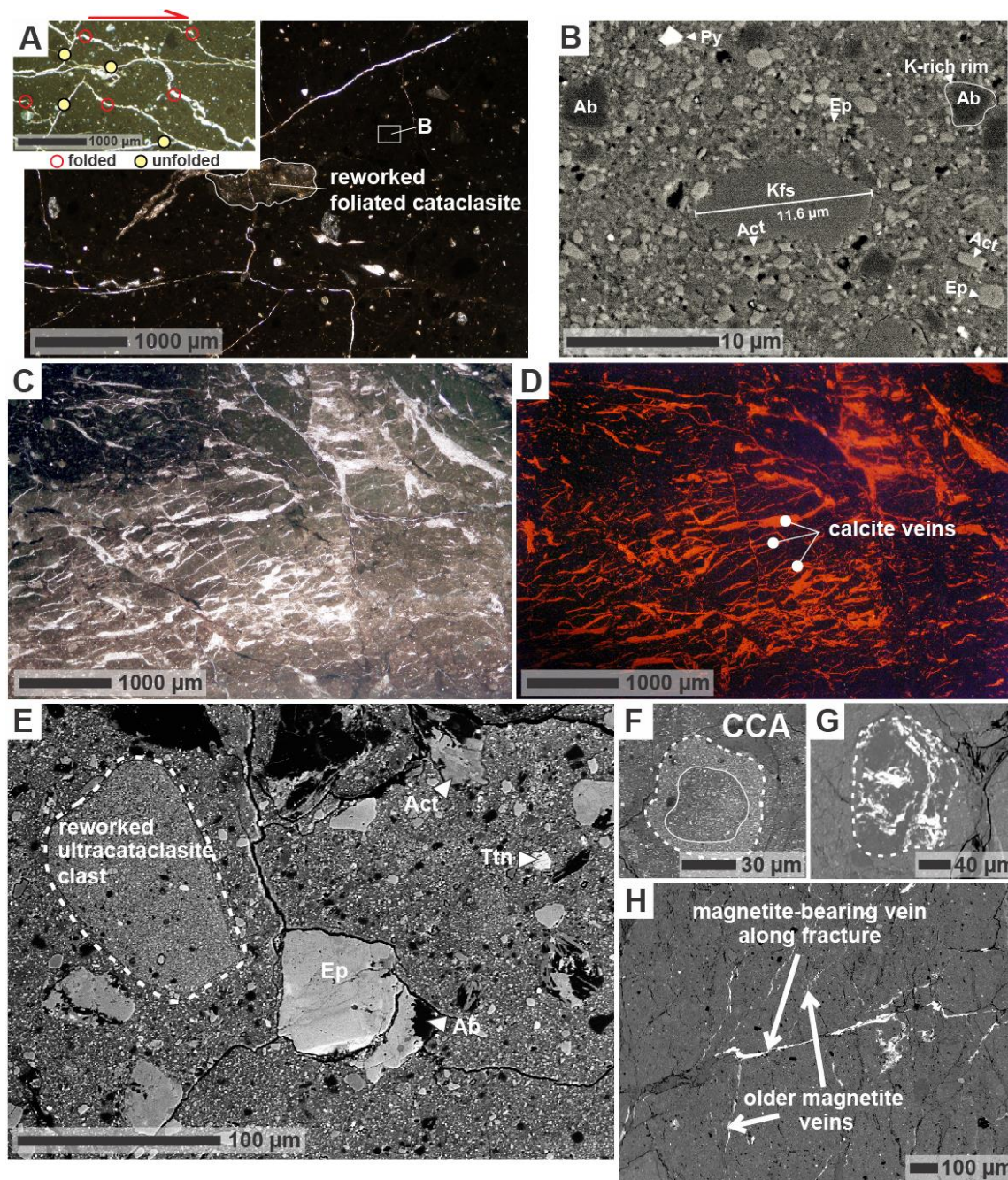


Figure 6. Ultracataclasite samples. A) Optical photomicrograph (plain light) of ultracataclasite sample PNG15-50B. Inset shows microfolding of backward-to-shear-inclined calcite veins (red circles) and necking or lack of folding of forward-inclined veins (yellow circles). B) Backscatter electron image (BSE) of ultracataclasite shown in (A). Note authigenic K-feldspar grain. C) Optical photomicrograph (plain light) of ultracataclasite sample PNG16-142D. Numerous calcite veins (white color) cross-cut the dark-colored, ultrafine-grained clay-rich matrix. D) Optical cathodoluminescence of area in (C) highlights calcite veinlets (orange) cross-cutting the ultracataclasite matrix. E) BSE image of ultracataclasite PNG16-142D. Older ultracataclasite clasts are reworked and show a higher concentration of K relative to the surrounding matrix (Supporting Information Figure S2.4). Mafic mineral clasts are up to 50 μm in diameter. F) BSE image of a clast cortex aggregate (CCA) that occurs locally in ultracataclasite samples (PNG16-142D). G) BSE image of ultracataclasite porphyroclast reworked into younger ultracataclasite PNG16-142D. The fragment contains magnetite-bearing veins (white) swirled into the clast. H) BSE image of mutually cross-cutting magnetite-bearing veins in ultracataclasite PNG16-142D.

Cathodoluminescence microscopy reveals intensive calcite veining in some of the ultracataclasites (Figs. 6C, 6D). Calcite veinlets of <100 µm thickness are mostly unfractured. Instead, they are ductilely deformed in a directionally-dependant manner that resembles calcite veins in the foliated cataclasites. Veinlets that are backwards-inclined with respect to the shear sense are folded, whereas those that are forward-inclined are unfolded and planar (Fig. 6A, inset). This contrasting veinlet geometry suggests that veinlet stress was imposed by normal sense shearing in the weaker, surrounding matrix.

The matrix consists predominantly of corrensite (mixed-layer chlorite-trioctahedral smectite) and/or saponite (trioctahedral smectite; Supporting Information Table S7). The matrix is also enriched in potassium (K-) feldspar relative to the foliated cataclasites and mylonites (Supporting Information Table S1.1). K-feldspar grains are >0.5 µm and up to ~12 µm in diameter, subhedral, unfractured, and in part replace albite (Fig. 6B). The observed increase of K and reduction in Na relative to the underlying foliated cataclasite, and growth of K-feldspar might be related to consumption of albite by the reaction:



We infer that the K-feldspar grains grew authigenically in the ultrafine-grained corrensite- and saponite-rich matrix of the ultracataclasite. The matrix encloses some ultracataclasite clasts that appear to have been derived from other parts of the same unit. The clasts are up to 100 µm in size, rounded and rarely fractured (Fig. 6E), and occasionally coated with an outer cortex (or swirled into the clast) of smectite or magnetite (Figs. 6F, 6G). These inherited fragments of ultracataclasite are generally more K-rich than the surrounding ultracataclasite host rock in which they are embedded (Supporting Information Fig. S2.4).

Some ultracataclasite samples contain distinctive magnetite-bearing clasts and veins (Figs. 6G, 6H). SEM-EDS analysis show that the multiple generations of magnetite-bearing veins (~20–60 µm-thick) cross-cut each other. Some veins contain magnetite ±maghemite grains <1 µm in size (Fig. 6H). Temperature-dependent magnetic susceptibility experiments on one of these ultracataclasite samples exposed just south of the Mai'iu fault trace (Supporting Information S5 for method and results) indicate a magnetic susceptibility of $\sim 13 \times 10^{-6} \text{ m}^3 \text{ kg}^{-1}$ and Curie temperatures between $T=580^\circ\text{C}$ and $T=645^\circ\text{C}$ for the magnetic fraction of this rock (Fig. 7). These results suggest the presence of cation-deficient magnetite (i.e., magnetite slightly oxidized to maghemite), an inference that also accords with our EDS data (Özdemir & Banerjee, 1984; Dunlop & Özdemir, 1997). Based on the similarity between the heating and cooling curves of the magnetic susceptibility experiment, the Curie temperatures and our EDS analyses, we infer that the principal magnetic mineral in the ultracataclasite is a stable (reversible), single domain (fine grained) magnetite.

Temperature-dependent magnetic susceptibility of an ultracataclasite

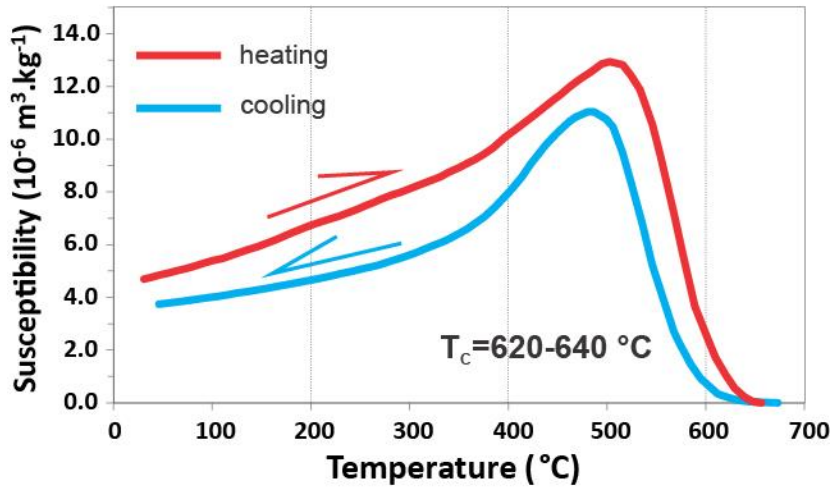


Figure 7. Curves of temperature dependant magnetic susceptibility for ultracataclasite sample PNG16-142D. The red and blue lines denote heating and cooling, respectively, from 40°C to 700°C and vice versa. T_C refers to the Curie temperature. A detailed explanation of the data curves can be found in the Supporting Information S5.

4.1.4 Gouges

In contrast to the underlying fault rock units, all four analysed gouge samples are devoid of calcite veins, although they do contain clasts of calcite or dolomite that were probably reworked from older veins. A foliation is not optically visible in the gouges. The gouge samples contain angular to sub-rounded mono- and polyphase clasts of epidote ($\varnothing \approx 4 \pm 3 \mu\text{m}$), actinolite ($\varnothing \approx 4 \pm 3 \mu\text{m}$), titanite ($\varnothing \approx 3 \pm 2 \mu\text{m}$), and albite ($\varnothing \approx 3 \pm 2 \mu\text{m}$), as well as clinopyroxene, quartz and calcite ($< 2 \mu\text{m}$) embedded in a phyllosilicate matrix (Figs. 8A, 8C). Based on XRD and EDS data, the 2 μm fraction of this matrix consists mainly of saponite (Supporting Information Table S7; see also Biemiller et al., submitted). Polyphase clasts are up to 1 cm in diameter and include fragments of mylonite, foliated cataclasite, and fine-grained K-rich fault rocks that resemble the ultracataclasite in texture and composition (Figs. 2G; 8A, 8B, 8D; Supporting Information Tables S1.2, S1.3). Some of the K-rich clasts show an enhanced porosity not seen in the ultracataclasites (Fig. 8D).

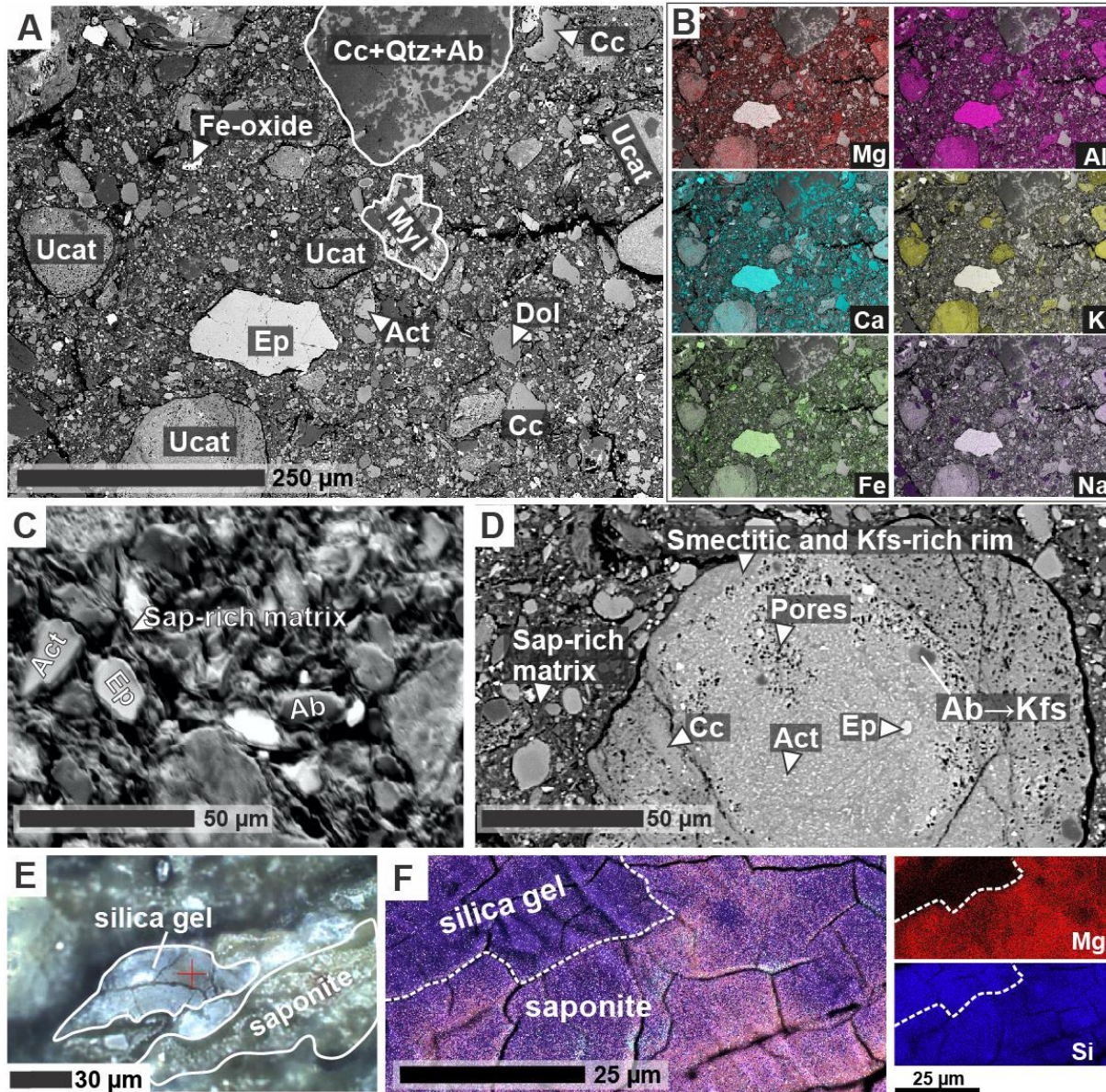


Figure 8. Gouge samples. A) Backscatter electron (BSE) image of gouge sample PNG14-33. This gouge contains reworked fragments of the structurally underlying fault rocks including ultracataclasites (ucat), mylonites (myl) and albite domains (light colored folia) of the foliated cataclasites. B) Element maps of (E) at reduced scale. The potassium (K) map highlights the K-rich ultracataclasite fragments. The magnesium (Mg) map highlights the saponite-rich gouge matrix. C) Forescatter diode image of the gouge microstructure with mono- and polyphase clasts “floating” in a porous saponite-rich matrix. D) BSE image showing a close-up of a K-rich, porous ultracataclasite clast. The ultracataclasite clast has a smectitic and K-feldspar-rich rim. E) Optical photomicrograph of a silica-rich domain adjacent to saponite (PNG14-19). F) EDS layered elemental map (Si and Mg) highlighting the transition from saponite to the silica-rich domain in PNG14-19.

The gouges contain trace amounts of dolomite and chromite (based on EDS analysis)—two minerals strongly associated with hangingwall ultramafic rocks. Furthermore, XRF analyses show that the gouges contain elevated concentrations of Cr and Ni compared to the mafic schists or mylonites in the footwall of the SDM (Supporting Information Table S8.1). Some gouges contain optically isotropic, tens of μm -thick silica-rich domains or patches (Fig. 8E). Figure 8F shows the diffuse nature of the transition from saponite to a silica-rich domain.

550 These relationships and the proximity of the silica phase to cracks and fractures in the samples
551 suggest that the silica is an alteration product of saponite and/or it has precipitated together with
552 saponite from hydrothermal fluids.

553 4.1.5 Hangingwall conglomerate and fault faceted cobbles

554 On the inactive segment of the Mai'iu fault, the principal displacement surface of the
555 Mai'iu fault forms the uppermost contact of the fault rock sequence. This planar, mm-thick
556 contact places unmetamorphosed Gwoira Conglomerate in the hangingwall against the gouges in
557 the footwall. The principal displacement surface truncates cm- to dm-sized clasts in the Gwoira
558 Conglomerate, forming mirror-like facets on those mostly gabbroic clasts. One faceted cobble of
559 dolerite was analyzed by SEM and TEM (Fig. 9). The goal was to describe the composition,
560 thickness and grain-size of the mirror-like surface and its fine striae. The analyzed TEM foil was
561 cut perpendicular to the shiny surface (Fig. 9D).

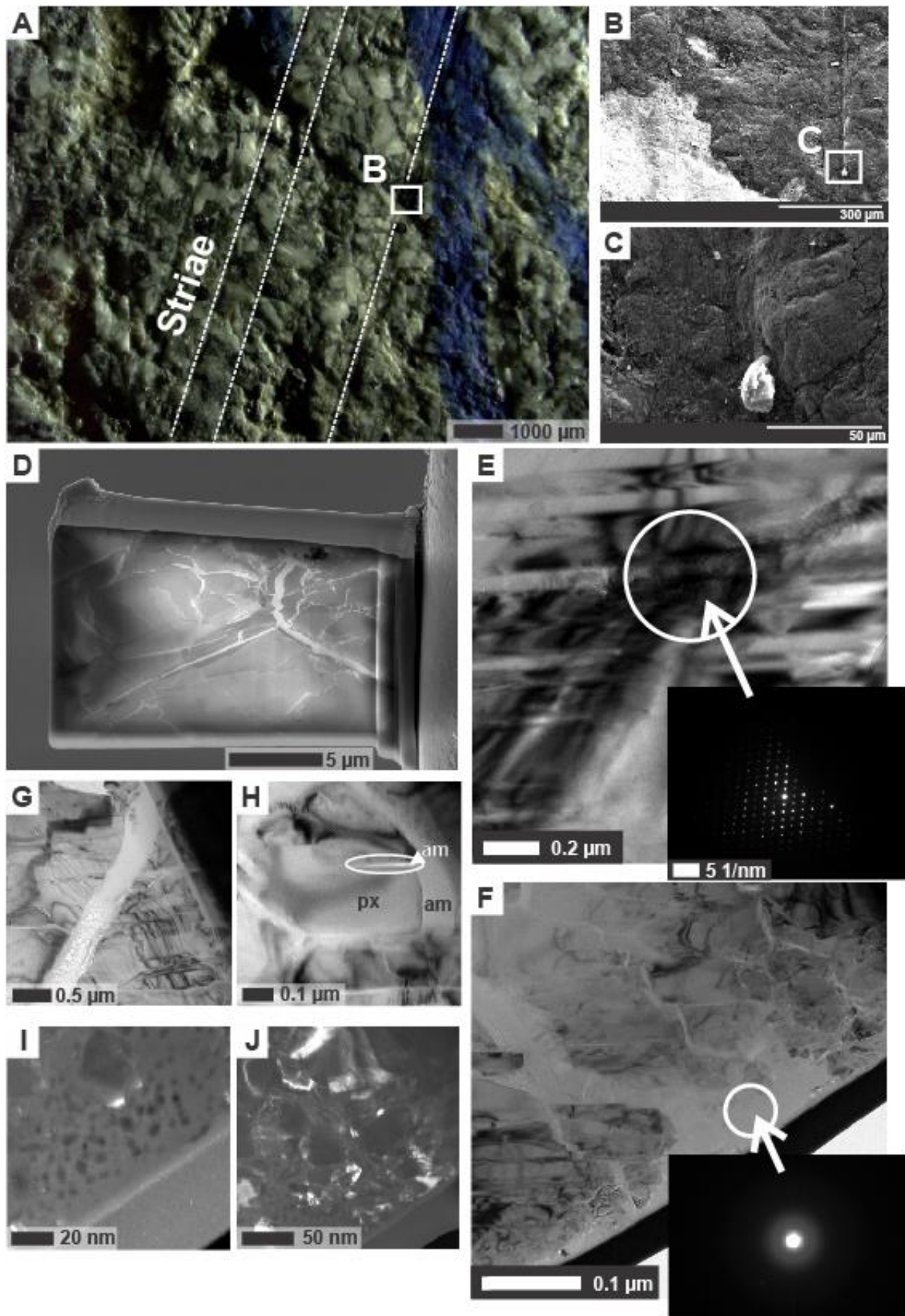


Figure 9. Gwoira Conglomerate dolerite cobble with nanograin coating. A) Optical photomicrograph (reflected light) of the cobble surface that was truncated by the fault. The surface is abraded by NNE-trending striae. B) Secondary electron image of the striation in (A). C) Close up of (B) showing a groove lineation behind a quartz asperity on a pyroxene grain. D) Focused ion beam (FIB) sample cut perpendicular to the fault (nanograin) surface. Amorphous vein material from the fault surface can be seen cutting across host material. E) TEM brightfield image of host material (pyroxene) comprising lamellae of clino- and orthopyroxene (inset diffraction pattern). F) TEM brightfield image of the shiny surface. Diffraction pattern (inset) illustrates that vein material and the surface are amorphous. G) Cross-cutting amorphous veins in host pyroxene. Beam damage can be seen as holes. H) Veinlet network and amorphous material surrounding, and injected into, a pyroxene grain. I-J) Darkfield TEM images. I) Polished surface of the truncated cobble. Dark spots in the TEM image are holes due to beam damage, suggesting that the amorphous material coating of the mirror surface volatilized under the high voltage current and is hydrous. J) Lower magnification image of (I) demonstrating continuity of the amorphous surface.

Striations on facet surfaces trend subparallel to the inferred NNE slip direction of the fault. Figures 9A–C show the striated surface of the analyzed dolerite including a groove lineation etched into a clinopyroxene-grain by a quartz fragment. The TEM analysis reveals that the mirror surface on the facets is a 2 μm -thick layer of amorphous material mainly consisting of Al and Si (Fig. 9I–F). The TEM images show multiple veins of this amorphous material emanating from the fault-parallel layer and injecting discordantly across host pyroxene grains in the truncated clast (Figs. 9G, 9H).

4.2 Chlorite geothermometry of the fault rocks

More than 100 chlorite grains (270 microprobe measurements) in 12 samples of mylonite and foliated cataclasite from eight localities in the Mai'iu fault zone were analysed. Our analyses targeted chlorite grains infilling syntectonically created microstructural sites, including: (a) in the mylonites, asymmetrical (normal sense) strain shadows and shear bands as well as pulled-apart necks between boudins of epidote and albite; (b) in the foliated cataclasites, dark chlorite-rich folia or C' normal-sense shear bands or ultracataclasite bands; and (c) in both the mylonites and foliated cataclasites, little deformed chlorite veins that cross-cut the foliation and/or pseudotachylite veins. The results of estimated chlorite formation temperatures versus the fraction of chlorite ($X=1$ is pure chlorite) to “swelling” component ($X=0$ is saponite) are shown in Figure 10.

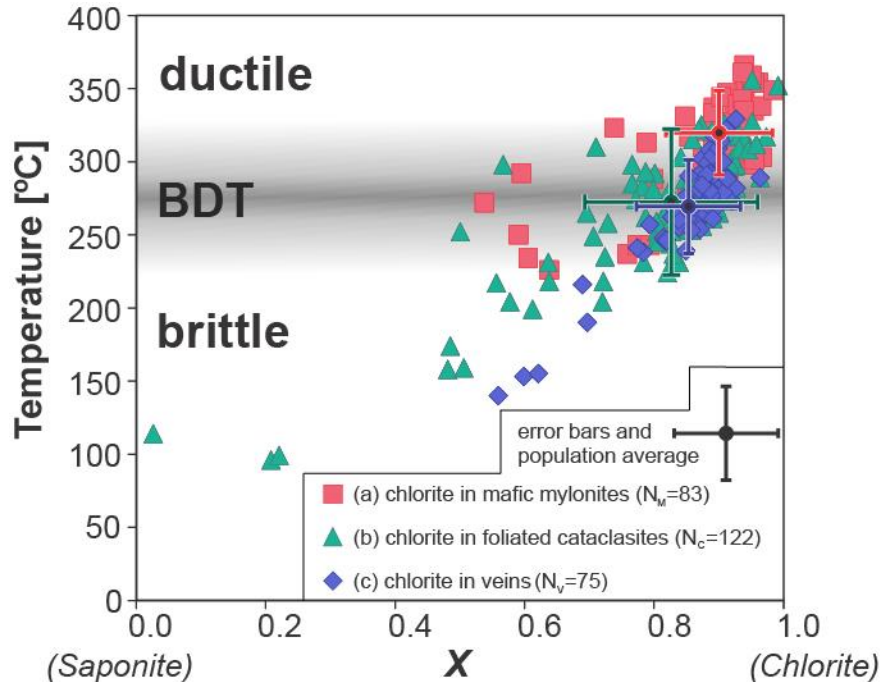


Figure 10. A plot of chlorite formation temperatures (calculated using the geothermometer by Cathelineau, 1988) versus X (the proportion of chlorite to swelling component after the method by Wise; see Bettison & Schiffman, 1988) for syntectonic microstructures in mafic mylonites and foliated cataclasites and chlorite veins cross-cutting these units (see text for explanations). The crosses indicate average values with 1σ error for estimated temperatures and chlorite proportion (X).

Chlorite geothermometry yields temperatures from: (a) 226°C to 366°C with an average of 310 ± 31 °C (1σ) in syntectonic sites in mylonites; (b) 158°C to 356°C with an average of 273 ± 46 °C (1σ) in syntectonic sites in foliated cataclasites; and (c) 140°C to 329°C with an average of 270 ± 34 °C (1σ) in little-deformed chlorite-filled veins cross-cutting both mylonite and foliated cataclasite. Nearly pure chlorite (clinochlore) is observed in all the mylonite samples ($X > 0.85$), whereas mixed-layer smectite-chlorite to saponite ($X < 0.50$) occurred in the dark folia of some of the foliated cataclasites. Overall there is an increase in “swelling” component (smaller X value) as the calculated temperature decreases. Following the recommendation of Bevins et al. (1991), we excluded the 12 chlorite compositional measurements for which $X < 0.55$ in our calculation of the average chlorite formation temperature for that unit. The shaded area in Figure 10 (labelled “BDT”) indicates the overlap between the estimated temperatures in the mylonite samples and the later, cross-cutting chlorite veins.

5 Discussion

5.1 Mai’iu fault structure and fault rock assemblage

The Mai’iu fault exposes mafic mylonitic rocks that have been exhumed from $\sim 25 \pm 5$ km depth at peak metamorphic conditions of $T = 425 \pm 50$ °C and $P = 5.9\text{--}7.2$ kbar (based on pseudosection modelling of EPMA mineral chemistry data, Daczko et al., 2009). The late Neogene and younger fabrics in the mylonitic unit were later overprinted in the narrower and structurally overlying < 3 m thick fault rock sequence composed of (from bottom to top): foliated cataclasite, ultracataclasite and gouge (Fig. 2). The upper mylonite and adjacent foliated

cataclasite units are cross-cut by several generations of chlorite, calcite and pseudotachylite veins, many of them ductilely deformed (Figs. 2, 3, 4). The brittle fault rocks (ultracataclasites and gouges) have a NNE-trending striation that is parallel to the ductile stretching lineation in the mylonitic rocks, and all fault rock units share the same normal shear sense. The fault rock units become thinner structurally upward, and each unit overprints the underlying one. Together, these observations record a progressive localization of slip that advanced structurally upward in time, and culminated with slip along the sharp and planar principal displacement surface at the base of the unmetamorphosed upper plate.

The estimated chlorite formation temperatures (Fig. 10) decrease from the mylonite (226–366°C) to the foliated cataclasite unit (158–356°C). We relate the wide temperature range of the foliated cataclasite, especially some very high estimated temperatures in that unit, to reflect the largely inherited nature of the mylonitic rock that was reworked into that younger, partially brittle fault rock (Fig. 4B). We interpret the overlap in estimated temperatures between the mylonites and late-stage chlorite veins that cut both it and the foliated cataclasite unit to indicate a temperature range of 226°C to 329°C at the onset of brittle fracturing (Fig. 10). The mineral transformation of chlorite to mixed-layer smectite-chlorite (Fig. 10) and the neoformed corrensite in the ultracataclasite unit indicate sub-greenschist-facies temperatures of ~150–225°C in this fault unit (e.g., Robinson et al., 2002; Surace et al., 2011; Moore et al., 2016). Furthermore, we suggest that saponite in the gouges (XRD data, Supporting Information Table S7.1) was stable at temperatures <150°C (e.g., Lockner et al., 2011; Richard et al., 2014; Boulton et al., 2018). Thus the fault rock sequence and its associated temperatures track a temporal evolution of cooling and embrittlement of the footwall together with progressive localization of brittle slip during exhumation across the BDT and to the Earth's surface.

The Mai'iu fault dips 15–24° along its trace but steepens northward to 30–40° at 12–25 km depth as indicated by a corridor of microseismicity down-dip of it (Abers et al., 2016; Fig. 1C). From these observations, we infer that the Mai'iu fault has a convex-upward geometry not only on the exhumed and abandoned southern part of the fault, but also on the active part of the fault in the subsurface to the north, a curvature that we attribute to operation of rolling hinge-style deformation (Spencer, 1984; Spencer, 2010; Mizera et al., 2019). The convexity, structure, fault rock assemblage, and some deformation mechanisms for the Mai'iu fault resemble those of other continental detachment faults (e.g., Platt et al., 2015; Cooper et al., 2017), but an unusual aspect of the Mai'iu fault is that its footwall rock type is primarily metabasaltic. The next section outlines several deformation mechanisms, both seismic and aseismic, that we infer were active in these mafic rocks as they were exhumed by slip on the Mai'iu fault (Fig. 11).

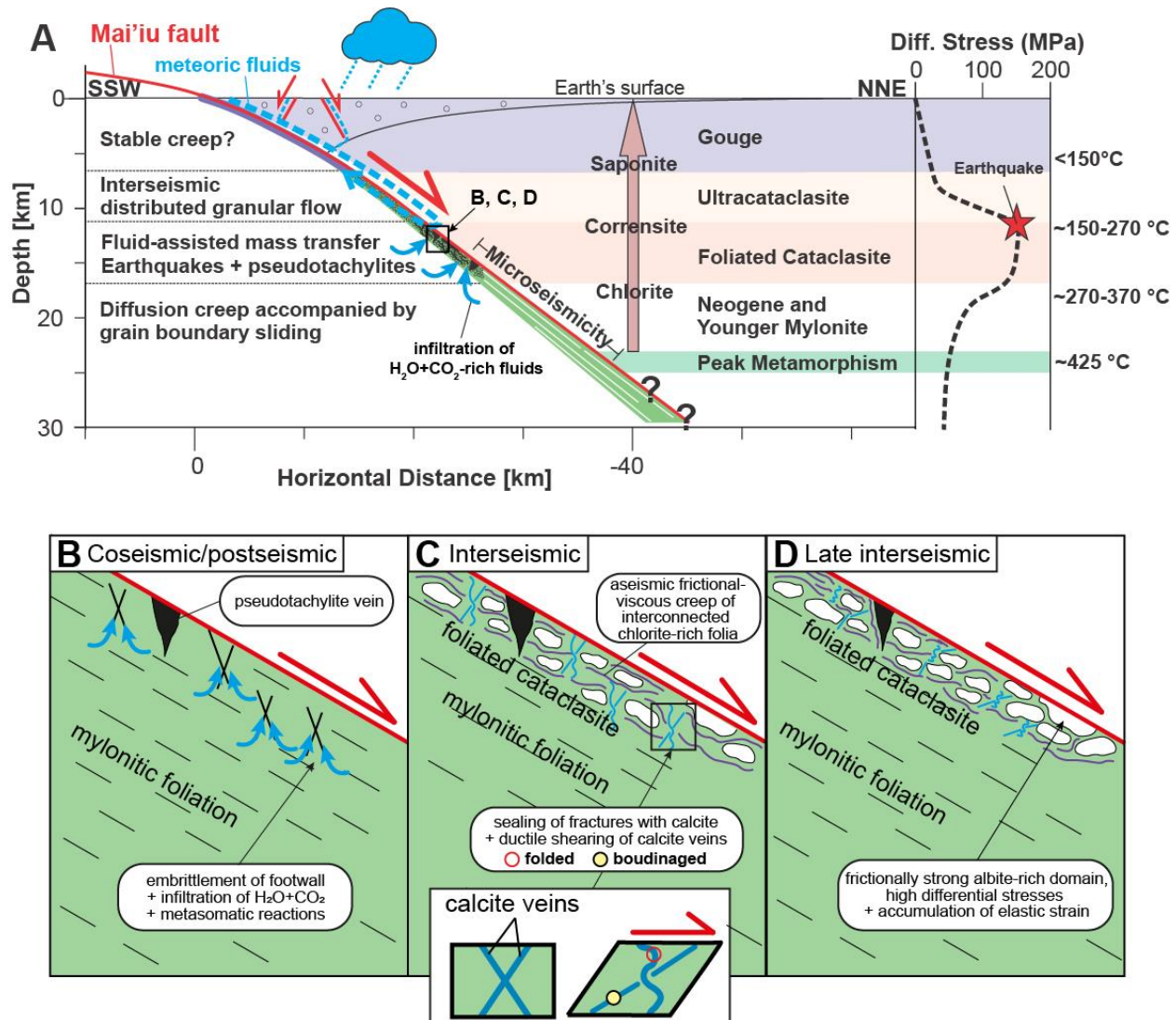


Figure 11. A) Profile across the Mai'iu fault and schematic spatiotemporal changes of deformation mechanisms interpreted in the context of the seismic cycle (e.g., Sibson, 1992). Blue arrows: influx of a chemically active fluid phase (H₂O + CO₂ rich). Mauve arrow with Chlorite, Corrensite, Saponite: Stability and change of these minerals as a function of depth. Microseismicity range is based on Abers et al. (2016). Schematic curve of maximum (static) differential stress versus depth for the Mai'iu fault is based on Mizera (2019). Red star on this strength-curve indicates the depth of dated pseudotachylite veins assuming a dip slip rate of ~10 mm/yr and a convex-upward shaped fault dipping 30–40° at depth. B-D) Schematic evolution of the rheology in the foliated cataclasites, active at a depth range corresponding to T=150 to 270°C, approximately 8 to 15 km. B) Brittle fracturing of the mafic mylonites and/or foliated cataclasites increases the permeability of the fault core, leading to the infiltration of H₂O + CO₂-rich fluids and reaction R1. Short black lines highlight open fractures (Coseismic/postseismic). C) Time-dependent and stress-dependent diffusive mass transfer processes within the foliated cataclasites ultimately lead to the development of interconnected chlorite-rich folia, promoting creep by stable frictional sliding in the chlorite-rich folia. Open fractures are sealed with hydrothermal calcite, and the calcite veins are ductilely sheared during interseismic periods (Interseismic). D) Gradually, precipitation of albite, calcite and quartz from an intergranular fluid phase in fractures and pores cement and strengthen the foliated cataclasites, thus promoting elastic strain accumulation (Late interseismic).

5.2 Evolution of deformation mechanisms during shearing of a metabasaltic footwall

5.2.1 Late Neogene and younger mylonites, precursor shear zone and fault reactivation

We do not observe any evidence for intracrystalline deformation of the primary mineral assemblage (epidote, actinolite, titanite, and albite) of the metabasaltic mylonites. Instead, we observe the following microstructures in these rocks (Fig. 3): (a) an average grain size of 6–35 μm ; (b) straight phase boundaries between epidote, actinolite and titanite grains and other phases along alignments that span a distance of several grain widths (Fig. 3B); (c) phase-boundary parallel grain offsets (predominantly epidote, actinolite and titanite) along these straight phase boundaries; (d) chemical zonation of epidote grains (Fig. 3B); (e) a strong CPO of non-plastically deformed actinolite grains (Fig. 3C); and (f) a weak to random CPO of albite.

From these observations, we infer that shearing in the mylonites was controlled by diffusion creep accompanied by grain-boundary sliding (GBS) (cf. Aspiroz et al., 2007; Getsinger et al., 2013; Elyaszadeh et al., 2018). The strong CPO of actinolite in the mylonites resembles that described for clinoamphiboles in other shear zones of greenschist- to amphibolite-facies metabasites (Aspiroz et al., 2007; Getsinger et al., 2013; Getsinger & Hirth, 2014). These authors attribute strong preferred orientations in amphiboles to diffusion creep accompanied by rigid-body rotation in an otherwise weak (plagioclase-rich), fine-grained matrix. Rigid-body rotation of actinolite in our rocks is consistent with widespread microfolding of the mylonitic foliation and fracturing of acicular actinolite grains (Fig. 3A, inset). Diffusion creep accommodated by anisotropic dissolution and precipitation of amphibole may also contribute to a strong CPO of amphibole (Pearce et al., 2011), and both processes are not mutually exclusive.

Based on the fine grain size of the mafic minerals, the strong shape preferred orientation (CPO and SPO) of actinolite, the syntectonic growth of chlorite (secondary phase admixture), we suggest that grain-size-sensitive creep was an important weakening mechanism in the mylonites. The fine grain size and preferred orientation of actinolite increases the cumulative surface area of the grains and decreases mean interparticle distances (e.g., Herwegh et al., 2011 and references therein), both of which would promote rates of diffusion creep. Newly grown interstitial chlorite may have helped to overcome local strain incompatibilities between grains (cf. Behrmann, 1985; Stünitz & Tullis, 2001; Speckbacher et al., 2013) and limit grain growth (Herwegh et al., 2011; Kilian et al., 2011; Menegon et al., 2015).

The transition from the precursor, non-mylonitic schist to the overlying Neogene and younger mylonites is marked by: (a) rotation of the stretching lineation from NW to NNE trends (Little et al., 2019); (b) a strengthening of the mafic fabric (especially the increase in CPO of actinolite, Fig. 5B); and (c) a change from top-to-the-south (thrust sense) to top-to-the-north (normal sense) shear fabrics (Figs. 2B, 2C). Both the non-mylonitic schist and the mylonites have similar fine grain sizes (Fig. 5B; Supporting Information Table S4.1 to S4.4) indicating that the footwall of the Mai'iu fault was pre-conditioned for grain size sensitive (GSS) creep prior to the onset of extension when the slip-sense on the fault was reversed. In particular, the Mai'iu fault inherited the pre-existing contrast between these fine-grained mafic rocks in the footwall and the coarse-grained ultramafic rocks (predominantly harzburgite and minor serpentine; Smith & Davies, 1976) of the Papuan Ultramafic Belt in the adjacent hangingwall. At the time of extensional fault inversion, this fault contact dipped $>44^\circ$, not only at depth but also at the surface, where the oldest hangingwall sediments onlapped against the fault scarp (Mizera et al., 2019; Webber et al., 2020).

Geodynamic models have explored conditions under which a preexisting, failed continental subduction margin may evolve into a domal metamorphic core complex after changes in tectonic boundary conditions (e.g., Biemiller et al., 2019). According to these, extensional inversion is most likely if the precursor thrust is: (1) weak and/or strain softening (see also Lavier et al., 1999; Choi & Buck, 2012; Choi et al., 2013), and (2) originally moderately to steeply dipping (Biemiller et al., 2019). Our observations, together with other data for the Mai'iu fault (Little et al., 2019; Mizera et al., 2019; Webber et al., 2020), converge on a scenario of extensional inversion of the Owen-Stanley thrust shear zone, with slip on that inherited fault zone exhuming the footwall through a rolling-hinge process.

5.2.2 Formation of the foliated cataclasite and implications for a seismic cycle on the Mai'iu fault

The upward transition from mylonites to the foliated cataclasites is marked by: (a) bleaching of the greenschist-facies derived metabasalt (lighter in colour and less mafic than in the mylonites, Figs., 2C, 2D); (b) decreasing mean grain size (Fig. 5B) and increasing intensity of microfaulting and brecciation; (c) development of a mm- to cm-scale spaced foliation defined by alternating albite-rich light and chlorite-rich dark coloured folia (Figs. 2D, 4); (d) strong embayment and truncation of epidote and actinolite against neo-formed chlorite (Fig. 4E); (e) passive concentration and growth of chlorite and subordinate clays in interconnected dark folia; (f) abundant calcite veining and cementation of albite in light-coloured folia (Fig. 4D); (g) CPO weakening and randomization in actinolite (indicated by decreasing M-index; Figs. 4G, 5B); and (h) increasing occurrence and thickness of pseudotachylite veins (Figs. 2E, 4A). These microstructures lead us to infer that the spaced foliation in the foliated cataclasite unit formed during deformation by the coupled fluid-assisted dissolution of epidote and actinolite, mostly in the dark-coloured seams, where it was associated with growth and concentration of chlorite and subordinate clays; and precipitation of albite, calcite and quartz, mostly in the light coloured domains.

One effect of dissolution of epidote and actinolite was bleaching of the foliated cataclasite relative to the mafic mylonite from which it was derived. Although this is a fluid-assisted reaction, we did not find evidence for sustained high pore-fluid pressures in the foliated cataclasites. Emplacement of calcite veins indicate that fluid pressures were at times high enough to induce hydrofracturing (i.e., $P_f > \sigma_3$); however, fluid influx was not high enough to completely retrogress the metabasaltic mineral assemblage as observed in other MCCs such as the Moresby Seamount Detachment in the eastern Woodlark Rift (Speckbacher et al., 2012, 2013). We interpret temporal variations in fluid pressure, the formation and folding of the foliation in the foliated cataclasites, and multiple generation of pseudotachylite veins hosted in these rocks in the context of a seismic cycle-model as explained below (e.g., Sibson, 1992; Scholz, 2002; Figs. 11B-D).

Influx of a chemically active fluid phase (H_2O+CO_2) during embrittlement of the mylonitic rocks (maybe during earthquakes) promoted the dissolution of mafic minerals (coseismic/postseismic period in Fig. 11B). In metasomatic reaction R.1, actinolite and epidote react away, leaving residual chlorite \pm illite to accumulate in the dark colored folia. At the same time, the reaction products calcite and quartz were precipitated in dilation sites, particularly within the light-colored folia. Part of the reaction also involved dissolution of albite, diffusion of albite in an intergranular fluid, and re-precipitation of albite in dilation sites, especially in the

light-colored folia together with calcite and quartz. Compositional changes of albite after dissolution and re-precipitation were insignificant (Fig. 5A).

This mass transfer process (mineral transformation, diffusive mass transfer, and re-precipitation) ultimately led to the development of an interconnected chlorite-rich folia in the cataclasites; a case of paired reaction and textural softening (e.g., Stewart et al., 2000; Imber et al., 2001; Moore & Lockner, 2004; Collettini & Holdsworth, 2004; Richard et al., 2014). Aseismic creep, at least temporarily, was facilitated by stable frictional sliding in the chlorite-rich folia (interseismic; Fig. 11C; e.g., Jefferies et al., 2006; Collettini et al., 2009). This is in some ways similar to the pressure solution-accommodated sliding model (frictional-viscous flow) of Bos and Spiers (2002), where minerals are dissolved at sites of stress concentration and re-precipitated in pressure shadows. Natural and experimental observations indicate that the kinetics of diffusive mass transfer is maximized along boundaries between phyllosilicates and more soluble phases (Niemeijer & Spiers, 2005; Gratier, 2011; Richard et al., 2014 and references therein).

An explanation for the mm-scale differentiated foliation might be that the fluid activity of the precipitating minerals (albite, quartz and calcite) was insufficient to transport mobile elements large distances in the intergranular fluid. Thus, deposition occurred in nearby voids (e.g., Gratier et al., 2013). Precipitation of albite, calcite and quartz in fractures and pores strengthened the rock locally, especially in the light-coloured folia (e.g., Richard et al., 2014). Such reaction-strengthening would slow down rates of dissolution–precipitation creep (e.g., Rutter, 1983) by increasing the mass transfer distance (late interseismic period, Fig. 11D). Increased sealing of the fractures with calcite may have led to a positive feedback loop, whereby the well-cemented, feldspar-rich light-coloured folia formed frictionally strong asperities that accumulated stress elastically and ultimately yielded by brittle, cataclastic deformation (cf. Richard et al., 2014).

The spaced foliation in the foliated cataclasites is pervasively folded on the mm- to cm-scale, and is transected by multiple generations of calcite and pseudotachylite veins that appear less folded than that foliation (Fig. 4A). These cross-cutting relationships suggest that periods of slow creep were accommodated by slip along the phyllosilicate-rich folia. Periodically, the foliated cataclasites hosted localized seismic slip, which caused fracturing, grain-size reduction, and frictional melting. In other words, the rock experienced a mixed-mode style of slip that was variably seismic to aseismic (e.g., Collettini et al., 2011; Little et al., 2019). The spatial pattern of weakening (phyllosilicate enrichment and alignment, in the dark folia) and strengthening (calcite cementation and veining, in the light folia) caused the rock to become layered and mechanically anisotropic, a situation that contributed to development of fold instabilities along the spaced foliation fabric. Calcite veins reflect episodic periods of fluid inflow that may have influenced the activity and distribution of the different deformation mechanisms (Richard et al., 2014).

5.2.3 Grain-size reduction, hydrous alteration and slow-to-fast slip processes in the ultracataclasites

The transition from the foliated cataclasite to the ultracataclasite is marked by: (a) extreme grain-size reduction (Figs. 5B, 6B); (b) bulk chemical changes (e.g., loss of Na, Ca and gain of K, Mg; Supporting Information Table S1.1); (c) mineral transformation from chlorite to trioctahedral mixed-layer smectite-chlorite \pm corrensite to saponite and the K-feldspathization of albite (R. 2); (d) randomization of all CPOs in actinolite, epidote and titanite (Fig. 5B); and (e)

formation of K-feldspar and magnetite \pm maghemite (Figs. 6G, 6H, 7). We infer that the dark-coloured, unfoliated, and clay-rich ultracataclasite unit with its sub-angular to rounded mafic clasts was derived from brittle fragmentation of the footwall. Bulk chemical changes, K-feldspathization of albite and neocrystallization of corrensite and K-feldspar indicate hydrous alteration of the basaltic footwall (XRD data of bulk mafic fault rocks Supporting Information Table S7.1). The well-rounded shape of the ultracataclasite lithic clasts in the ultracataclasite, and especially the coated structure of those clasts (clast-cortex aggregates, CCA; Figs. 6E–G), suggest clast rotation during granular flow and accretion of clay material (e.g., Boutareaud et al., 2008; Han & Hirose, 2012; Rempe et al., 2014). Granular flow of the ultracataclasite matrix is also suggested by attitude-dependant stretching versus folding of calcite veinlets embedded in it (Fig. 6A)—a relationship that indicates distributed shearing in that matrix (Little et al., 2019).

We interpret the high magnetic susceptibility of $\sim 13 \times 10^{-6} \text{ m}^3 \text{ kg}^{-1}$ measured in one of the ultracataclasite samples from the Mai'iu fault (compared to the other Mai'iu fault rocks and Goropu Metabasalt; Watson, 2019) and the occurrence of abundant, nm-sized magnetite \pm maghemite in ultracataclasite samples (in veins, as coatings, and swirled into reworked ultracataclasite clasts) to have formed by the breakdown of predominantly Fe-bearing mixed-layer smectite-chlorite during frictional shearing (thermomechanical decomposition). This interpretation is supported by changes in rock magnetic properties in other fault zones associated with recent earthquakes (e.g., 1999 Taiwan Chi-Chi earthquake, e.g., Mishima et al., 2009; Wenchuan earthquake in Sichuan Province, China, e.g., Cai et al., 2019) and high-velocity frictional experiments on crushed siltstones (containing quartz with a matrix of clay minerals, such as illite, kaolinite, smectite, and chlorite; e.g., Tanikawa et al., 2007). The high-velocity frictional experiment by Tanikawa et al. (2007) showed that the bulk magnetic susceptibility is proportional to the frictional work applied and increases with displacement due to thermal decomposition of paramagnetic clays in the powdered siltstone. Both thermally and mechanically driven mineral transformation reactions contribute to an anomalously high magnetic susceptibility, similar to that observed in the Mai'iu fault ultracataclasite unit (Fig. 7; e.g., Tanikawa et al., 2008).

Frictional devolatilization of Fe-bearing smectite clay is expected at temperatures $>400^\circ\text{C}$ (Rowe & Griffith, 2015 and references therein). We did not observe breakdown of mixed-layer smectite-chlorite during the time-dependent magnetic susceptibility test; however, the test was performed under 1 atm and without any frictional work. Another possibility is that the magnetite was derived from external supersaturated hydrothermal fluids (i.e., external Fe-saturated fluids from ultramafic rocks in the hangingwall). This origin may be supported by the occurrence of magnetite along fractures in the ultracataclasites, but it does not explain the precipitation of single magnetite grains scattered within the fault rock or the magnetite nanograin coating around older ultracataclasite clasts (Supporting Information S5).

We infer that deformation of the ultracataclasite unit occurred at strain rates that varied with time. Hydrous alteration of the ultracataclasite matrix indicates that fluid inflow led to weakening of the matrix by retrogression of chlorite to corrensite (e.g., Moore, 2014). At the same time, cementation with unstable calcite would promote strengthening (e.g., Verberne et al., 2015). The observed suite of microstructures, including ductilely folded calcite veinlets, in the ultracataclasite unit indicate that periods of slow (probably aseismic) creep potentially alternated with fast (potentially seismic) slip events. CCAs similar to ones observed in our fault rocks have been reproduced in rotary shear experiments on frictionally heated granular material at seismic

velocities (Boutareaud et al. 2010, 2012). However, granular flow at a wide range of velocities can produce CCAs, even in the absence of thermal pressurization and fault rock fluidization at elevated temperature (Han & Hirose, 2012). While granular flow itself can facilitate CCA formation, the nanograin magnetite that coats clasts in the Mai'iu fault ultracataclasite appears to have originated from the thermal decomposition of Fe-bearing minerals such as corrensite during coseismic slip (Hirono et al., 2006; Mishima et al., 2006; Yang et al., 2012).

5.2.4 Frictionally weak fault gouges and fault-faceted surfaces of cobbles truncated by the principal displacement surface

The gouges contain recycled clasts from the underlying mafic footwall (ultracataclasite, cataclasite and mylonite fragments) and, from ultramafic rocks in the overlying hangingwall (dolomite and spinel-group minerals). This recycling is reflected by an increase in grain-size of mono- and polyphase clasts in the gouge relative to those in the underlying ultracataclasite (Fig. 8A). The recycled clasts in the gouges “float” in a fine-grained matrix dominated by saponite (Fig. 8C) and have random CPOs as indicated by a low M-index (Fig. 5B). Incorporation of ultramafic components into the gouge potentially promoted saponite-forming reactions (e.g., Moore & Rymer, 2012; Moore, 2014). Saponite is typically derived from the breakdown of chlorite and/or corrensite under declining temperatures. In mafic rocks, its formation requires fluid, and it consumes Mg, Fe, Al and (Ca + Na + K) derived from epidote, actinolite, albite (and, in our case potentially also the ultramafic hangingwall; e.g., Moore, 2014). Multiple phases of fluid flow might be recorded by our observation of saponitic domains overprinted by silica-rich ones (Figs. 8E, 8F).

The Pliocene alluvial conglomerates of the Gwoira Conglomerate (<3 km thick; Webber et al., 2020) and Quaternary deposits in the hangingwall form permeable pathways for the flow of meteoric fluids. Such fluids may have significantly altered and weakened the fault gouges in the shallowest part of the Mai'iu fault zone (Fig. 11A; Little et al., 2019). Experimental data on saponite-rich gouges (Carpenter et al., 2012; Moore et al., 2016; Boulton et al., 2018; Biemiller et al., submitted) indicate a weak coefficient of friction ($\mu < 0.2$) and velocity-strengthening behaviour (subject to aseismic stable sliding) across a wide range of sub-seismic sliding velocities, temperatures, and effective normal stresses. However, at coseismic slip velocities (> 0.1 m/s), velocity-strengthening minerals such as saponite do not necessarily prevent large earthquake rupture propagation (e.g., Di Toro et al., 2011; Faulkner et al., 2011; Boulton et al., 2017).

Our documentation of amorphous, mirror-like surfaces (nanograin coating) on the fault-faceted surfaces of cobbles truncated by the principal displacement surface may reflect seismic slip at shallow depths (Figs. 1K; 9)—although this interpretation is debatable (e.g., Verberne et al., 2014; De Paola et al., 2015 and references therein). In some laboratory experiments, a nanograin coating was produced by extreme grain comminution at seismic to subseismic creep velocities (e.g., Verberne et al., 2014). To assess whether the nanograins may have formed by comminution or shear heating, we calculated the minimum grain size that can be achieved by grinding (the grinding limit) for a basaltic rock, plagioclase and quartz based on fracture toughness (K_{IC}) and flow stresses at zero °K ($\hat{\tau}_0$; equation 13 in Sammis & Ben-Zion, 2008). The estimated minimum grain sizes are $> d_{\min \text{Basalt}} = 268$ nm, $> d_{\min \text{Plag}} = 53$ nm and $> d_{\min \text{Quartz}} = 86$ nm, respectively ($d_{\min \text{Quartz}}$ was calculated by Sammis & Ben-Zion, 2008; Mizera, 2019). This estimation is imprecise due to the uncertainties in material properties (Sammis & Ben-Zion,

2008), but it suggests that the interpreted amorphous mirror-like coating on the cobble-surfaces (Figs. 9F, 9I, 9J) cannot be achieved by comminution alone. For this reason, we interpret that this nano-coating of amorphous material (Si and Al rich) and the injection veins (Figs. 9D, 9G, 9H) have been generated by frictional heating and slip along a narrow principal displacement surface (e.g., Oohashi et al., 2011; Smith et al., 2013; Rowe & Griffith, 2015 and references therein).

5.3 Strain rates during exhumational shearing of the Mai'iu fault

A maximum strain rate in the mafic mylonites that accommodated extensional slip on the Mai'iu fault can be calculated by the relation $\epsilon = \dot{u}/h$, where ϵ is the strain rate, \dot{u} the slip rate and h the thickness of the deforming zone (e.g., Rowe et al., 2011). Using the known fault dip-slip rate of ~ 10 mm/yr (Webber et al., 2018) and the width of the mylonites, which thin from ~ 60 m to as low as 1.5 m, calculated shear strain rates range from 5.3×10^{-12} to $2.1 \times 10^{-10} \text{ s}^{-1}$. Getsinger and Hirth (2014) showed that flow laws for wet plagioclase can be similarly applied to fine-grained amphibole. Applying experimentally derived diffusion creep flow laws for wet Ab_{100} (H_2O 0.2 wt.%) by Offerhaus et al. (2001), pure albite with an average grain size diameter of $\sim 15 \text{ }\mu\text{m}$ in the mylonites at temperature of $\sim 400^\circ\text{C}$ and differential stresses of $\sim 60\text{--}100 \text{ MPa}$ (Little et al., 2019; Mizera, 2019) is predicted to deform at strain rates of 1.5×10^{-13} to $\sim 2.5 \times 10^{-13} \text{ s}^{-1}$. This estimated strain rate is lower than that required to accommodate the full dip-slip rate. This shortfall may indicate that: (1) a natural polyphase mafic aggregate at greenschist facies conditions with its neoformed, interstitial chlorite (and with strong CPO and SPO) is weaker in diffusion creep than that predicted by extrapolations of laboratory experiments on wet albite (Little et al., 2019); or (2) the sheared thickness of the mylonite unit was thicker than assumed above.

To accommodate the Mai'iu fault's full slip rate in the $\sim 1.5\text{--}3.0$ m-wide foliated cataclasites by aseismic creep of the interconnected chlorite-rich folia would require a bulk strain rate of 1.1×10^{-10} to $2.1 \times 10^{-10} \text{ s}^{-1}$, but this is likely higher than the actual rate of long-term, frictional-viscous pressure solution creep (e.g., Bos & Spiers, 2002; Imber et al., 2008). Aseismic creep may locally be impeded where chlorite-rich folia become locked against stronger albitic domains enlarging through precipitation and/or not dissolving fast enough (dissolution-limited), perhaps causing them to deform cataclastically (e.g., Richard et al., 2014). Such load transfer into the albite-rich layers might have caused elastic strain to increase and creep rates to reduce in the foliated cataclasites (i.e., case of partial locking, Fig. 11D; see Biemiller et al., submitted). Ductilely deformed calcite and pseudotachylite veins in the foliated cataclasite unit (Fig. 4A, inset) are strong evidence that some slip in this unit was seismic, and that fast-slip events were followed by postseismic and/or interseismic creep.

5.4 Seismic slip along an active low-angle normal fault

Overall, several lines of evidence suggest that some slip on the Mai'iu fault was seismic. These include: (1) pseudotachylite veins in mylonites and foliated cataclasites (Figs. 2E, 3E, 4A); (2) nm-sized magnetite \pm maghemite grains in veins cross-cutting the ultracataclasite matrix and wrapping older ultracataclasite clasts (Figs. 6G, 6H); and (3) mirror-like surfaces on hangingwall cobbles truncated by the fault and coated with amorphous material (Fig. 9). The numerous exposed, 5–40 mm thick pseudotachylite veins as well as brittle faults cross-cutting the spaced foliation in the foliated cataclasites indicate that aseismic fluid-assisted mass transfer

was periodically punctuated by earthquakes. During earthquakes, slip on the the propagating rupture may have led to the thermomechanical breakdown of Fe-bearing minerals (predominantly mixed-layer smectite-chlorite in the ultracataclasites) by frictional heating to form magnetite-bearing veins (e.g., Cai et al., 2019). Dated pseudotachylite veins hosted by the foliated cataclasite unit yield $^{40}\text{Ar}/^{39}\text{Ar}$ ages as young as ~ 2.2 Ma (Little et al., 2019). At the known slip rate of ~ 10 mm/yr on a $30\text{--}40^\circ$ dipping fault, such ages imply pseudotachylite generation at 10–12 km depth. We infer that the foliated cataclasite and its pseudotachylite veins formed in a relatively strong, moderately-dipping, mid-crustal domain of elevated differential stress where slip was accommodated by a mixture of seismic and aseismic slip (Fig. 11A). We interpret the corridor of microseismicity at 12–25 km depth (Abers et al., 2016) to reflect present-day aseismic creep (e.g., Chiaraluce et al., 2007, 2014; Vadacca et al., 2016) that is taking place in the down-dip, un-exhumed equivalents of the described mylonites and foliated cataclasites.

6 Conclusions

The Mai'iu fault zone, an extensional detachment formed from inversion of a pre-existing ophiolitic suture, developed in a pre-existing, fine-grained, footwall metabasaltic protolith. The upwardly narrowing arrangement of progressively lower-temperature fault rocks developed from this protolith display clear evidence that slip became progressively localized and more brittle as slip on the fault carried the footwall towards the surface. Microstructures in the fault rocks record transitions in dominant deformation mechanisms in metabasaltic rocks accommodating slip, and chlorite thermometry allows us to assign approximate temperatures to these transitions.

- Slip within the mylonites was accomplished by diffusion creep accompanied by rotation and grain-boundary sliding of pre-existing, fine-grained ($\sim 6\text{--}35$ μm in diameter) epidote, actinolite, chlorite, and albite at temperatures $>270\text{--}370^\circ\text{C}$ and strain-rates of 5.3×10^{-12} to 2.1×10^{-10} s^{-1} .
- At shallower levels on the fault ($T \geq 150\text{--}300^\circ\text{C}$), fluid-assisted mass transfer of albite, quartz and calcite led to mineral transformation reactions with continuous chlorite growth, creating a 1.5–3 m thick zone of foliated cataclasites. This zone deformed in part by aseismic frictional-viscous creep at a maximum strain rate of 1.1×10^{-10} to 2.1×10^{-10} s^{-1} .
- Build-up of elastic-strain in the foliated cataclasites eventually facilitated earthquakes propagation through them, as indicated by the injection of pseudotachylite veins. Later creep caused folding of those veins.
- The foliated cataclasites formed at $\sim 8\text{--}15$ km depth in a frictionally strong, mid-crustal part of the fault that dipped at least $\sim 30^\circ$. This zone maintained elevated differential stresses and deformed at slip rates that varied spatiotemporally from high (seismic) to low (aseismic).
- Slip in the shallower-formed ultracataclasite unit ($T \sim 150\text{--}225^\circ\text{C}$) was at least in part accomplished by distributed granular flow of the ultrafine-grained mafic minerals.
- At the shallowest crustal levels ($T < 150^\circ\text{C}$), clay-rich gouges contain abundant saponite, a velocity-strengthening, weak mineral ($\mu < 0.2$). Given sufficient areal

distribution on the fault plane, saponite gouges may have promoted aseismic slip on the shallowest dipping most poorly oriented part of the Mai'iu fault (dipping ~15–24°). In the light of our data, slip on the shallow Mai'iu fault does not present a mechanical paradox.

Acknowledgments, Samples, and Data

Marsden Fund grant VUW1310 provided financial support to conduct this research. We are grateful to Hugh Davies (University of Papua New Guinea) and Ian Smith (University of Auckland) for providing field book scans and discussions. We thank Susan Ellis, Samuel Webber, Jürgen Österle, Laura Wallace, Kevin Norton, and Daniel Stockli for field support and discussions. This work profited from discussions with André Niemeijer that helped to sharpen our thinking. Special thanks go to the many landowners, oral chiefs, elders, and citizens who granted us permission to study their land and who allowed us to stay in their villages or houses and were supportive with advice and help. We also thank our guides and carriers without whom this work would not have been possible.

All structural data can be obtained from Little et al. (2019) and Mizera (2019). All microstructural and geochemical data presented in this study are available through Mizera (2019).

References

- Abers, G. A., Mutter, C. Z., & Fang, J. (1997). Shallow dips of normal faults during rapid extension: Earthquakes in the Woodlark-D'Entrecasteaux rift system, Papua New Guinea. *Journal of Geophysical Research: Solid Earth*, 102(B7), 15301-15317.
- Abers, G. A., Eilon, Z., Gaherty, J. B., Jin, G., Kim, Y. H., Obrebski, M., & Dieck, C. (2016). Southeast Papuan crustal tectonics: Imaging extension and buoyancy of an active rift. *Journal of Geophysical Research: Solid Earth*, 121(2), 951-971.
- Anderson, E. M. (1951). The dynamics of faulting.
- Aspiroz, M. D., Lloyd, G. E., & Fernández, C. (2007). Development of lattice preferred orientation in clinoamphiboles deformed under low-pressure metamorphic conditions. A SEM/EBSD study of metabasites from the Aracena metamorphic belt (SW Spain). *Journal of Structural Geology*, 29(4), 629-645.
- Axen, G. J., & Bartley, J. M. (1997). Field tests of rolling hinges: Existence, mechanical types, and implications for extensional tectonics. *Journal of Geophysical Research: Solid Earth*, 102(B9), 20515-20537.
- Axen, G. J. (2004). Low-angle normal fault mechanics and crustal strength. In: *Rheology and Deformation of the Lithosphere* (ed. G. Karner), 46-91 (Columbia University Press, 2004).
- Axen, G. J. (2007). Research Focus: Significance of large-displacement, low-angle normal faults. *Geology*, 35(3), 287-288.
- Bachmann, F., Hielscher, R., & Schaeben, H. (2010). Texture analysis with MTEX—free and open source software toolbox. In *Solid State Phenomena* (Vol. 160, pp. 63-68). Trans Tech Publications Ltd.

- Behrmann, J. H. (1985). Crystal plasticity and superplasticity in quartzite; a natural example. *Tectonophysics*, 115(1), 101-129.
- Beiersdorfer, R. E., & Day, H. W. (1995). Mineral paragenesis of pumpellyite in lowgrade mafic rocks. *Low-Grade Metamorphism of Mafic Rocks: Boulder, Colorado*, Geological Society of America. Special Paper, 296, 5-27.
- Bercovici, D., & Ricard, Y. (2012). Mechanisms for the generation of plate tectonics by two-phase grain-damage and pinning. *Physics of the Earth and Planetary Interiors*, 202, 27-55.
- Bettison, L. A., & Schiffman, P. (1988). Compositional and structural variations of phyllosilicates from the Point Sal ophiolite, California. *American Mineralogist*, 73(1-2), 62-76.
- Bevins, R. E., Robinson, D., & Rowbotham, G. (1991). Compositional variations in mafic phyllosilicates from regional low-grade metabasites and application of the chlorite geothermometer. *Journal of Metamorphic Geology*, 9(6), 711-721.
- Biemiller, J., Ellis, S., Mizera, M., Little, T., Wallace, L., & Lavier, L. (2019). Tectonic inheritance following failed continental subduction: a model for core complex formation in cold, strong lithosphere. *Tectonics*, 38(5), 1742-1763.
- Bos, B., & Spiers, C. J. (2002). Frictional-viscous flow of phyllosilicate-bearing fault rock: Microphysical model and implications for crustal strength profiles. *Journal of Geophysical Research: Solid Earth* (1978–2012), 107(B2), ECV-1.
- Boulton, C., Yao, L., Faulkner, D. R., Townend, J., Toy, V. G., Sutherland, R., ... & Shimamoto, T. (2017). High-velocity frictional properties of Alpine Fault rocks: Mechanical data, microstructural analysis, and implications for rupture propagation. *Journal of Structural Geology*, 97, 71-92.
- Boulton, C., Barth, N. C., Moore, D. E., Lockner, D. A., Townend, J., & Faulkner, D. R. (2018). Frictional properties and 3-D stress analysis of the southern Alpine Fault, New Zealand. *Journal of Structural Geology*.
- Bourdelle, F., & Cathelineau, M. (2015). Low-temperature chlorite geothermometry: a graphical representation based on a T–R2+–Si diagram. *European Journal of Mineralogy*, 27(5), 617-626.
- Boutareaud, S., Calugaru, D. G., Han, R., Fabbri, O., Mizoguchi, K., Tsutsumi, A., & Shimamoto, T. (2008). Clay-clast aggregates: A new textural evidence for seismic fault sliding?. *Geophysical Research Letters*, 35(5).
- Boutareaud, S., Boullier, A. M., Andreani, M., Calugaru, D. G., Beck, P., Song, S. R., & Shimamoto, T. (2010). Clay clast aggregates in gouges: New textural evidence for seismic faulting. *Journal of Geophysical Research: Solid Earth*, 115(B2).
- Boutareaud, S., Hirose, T., Andréani, M., Pec, M., Calugaru, D. G., Boullier, A. M., & Doan, M. L. (2012). On the role of phyllosilicates on fault lubrication: Insight from micro-and nanostructural investigations on talc friction experiments. *Journal of Geophysical Research: Solid Earth*, 117(B8).

- 1057 Buck, W. R. (1990). Comment on “Origin of regional, rooted low-angle normal faults: A
1058 mechanical model and its tectonic implications” by An Yin, *Tectonics*, 9(3), 545–546,
1059 doi: 10.1029/TC009i003p00545.
- 1060 Bunge, H. J. (2013). *Texture analysis in materials science: mathematical methods*. Elsevier.
- 1061 Byerlee, J. (1978). Friction of rocks. *Pure and applied geophysics*, 116(4-5), 615-626.
- 1062 Cai, Y., Pei, J., Wang, H., Sheng, M., & Si, J. (2019). Paleo-earthquakes revealed by rock
1063 magnetic evidence from the Anxian-Guanxian Fault, Sichuan Province, China.
1064 *Tectonophysics*, 752, 68-80.
- 1065 Cairns, E. A., Little, T. A., Turner, G. M., Wallace, L. M., & Ellis, S. (2015). Paleomagnetic
1066 evidence for vertical-axis rotations of crustal blocks in the Woodlark Rift, SE Papua New
1067 Guinea: Miocene to present-day kinematics in one of the world's most rapidly extending
1068 plate boundary zones. *Geochemistry, Geophysics, Geosystems*, 16(7), 2058-2081.
- 1069 Carpenter, B. M., Saffer, D. M., & Marone, C. (2012). Frictional properties and sliding stability
1070 of the San Andreas fault from deep drill core. *Geology*, 40(8), 759-762.
- 1071 Cathelineau, M., & Nieva, D. (1985). A chlorite solid solution geothermometer the Los Azufres
1072 (Mexico) geothermal system. *Contributions to Mineralogy and Petrology*, 91(3), 235-
1073 244.
- 1074 Cathelineau, M. (1988). Cation site occupancy in chlorites and illites as function of temperature.
1075 *Clay minerals*, 23(4), 471-85.
- 1076 Chiaraluce, L., Chiarabba, C., Collettini, C., Piccinini, D., & Cocco, M. (2007). Architecture and
1077 mechanics of an active low-angle normal fault: Alto Tiberina fault, northern Apennines,
1078 Italy. *Journal of Geophysical Research: Solid Earth*, 112(B10).
- 1079 Chiaraluce, L., Amato, A., Carannante, S., Castelli, V., Cattaneo, M., Cocco, M., ... & Marzorati,
1080 S. (2014). The Alto Tiberina Near Fault Observatory (northern Apennines, Italy). *Annals*
1081 *of Geophysics*, 57(3).
- 1082 Choi, E., & Buck, W. R. (2012). Constraints on the strength of faults from the geometry of rider
1083 blocks in continental and oceanic core complexes. *Journal of Geophysical Research:*
1084 *Solid Earth*, 117(B4).
- 1085 Choi, E., Buck, W. R., Lavier, L. L., & Petersen, K. D. (2013). Using core complex geometry to
1086 constrain fault strength. *Geophysical Research Letters*, 40(15), 3863-3867.
- 1087 Collettini, C., & Sibson, R. H. (2001). Normal faults, normal friction?. *Geology*, 29(10), 927-
1088 930.
- 1089 Collettini, C., & Holdsworth, R. E. (2004). Fault zone weakening and character of slip along
1090 low-angle normal faults: insights from the Zuccale fault, Elba, Italy. *Journal of the*
1091 *Geological Society*, 161(6), 1039-1051.
- 1092 Collettini, C., Niemeijer, A., Viti, C., & Marone, C. (2009). Fault zone fabric and fault weakness.
1093 *Nature*, 462(7275), 907-910.
- 1094 Collettini, C. (2011). The mechanical paradox of low-angle normal faults: Current understanding
1095 and open questions. *Tectonophysics*, 510(3), 253-268.

- Collettoni, C., Niemeijer, A., Viti, C., Smith, S. A., & Marone, C. (2011). Fault structure, frictional properties and mixed-mode fault slip behavior. *Earth and Planetary Science Letters*, 311(3-4), 316-327.
- Collettoni, C., Tesei, T., Scuderi, M. M., Carpenter, B. M., & Viti, C. (2019). Beyond Byerlee friction, weak faults and implications for slip behavior. *Earth and Planetary Science Letters*, 519, 245-263.
- Cooper, F. J., Platt, J. P., & Behr, W. M. (2017). Rheological transitions in the middle crust: insights from Cordilleran metamorphic core complexes. *Solid Earth*, 8(1), 199.
- Cross, A. J. (2015). Microstructural evolution under non-steady state deformation in mid-crustal ductile shear zones (Doctoral dissertation, University of Otago).
- Daczko, N. R., Caffi, P., Halpin, J. A., & Mann, P. (2009). Exhumation of the Dayman dome metamorphic core complex, eastern Papua New Guinea. *Journal of Metamorphic Geology*, 27(6), 405-422.
- Daczko, N. R., Caffi, P., & Mann, P. (2011). Structural evolution of the Dayman dome metamorphic core complex, eastern Papua New Guinea. *Bulletin*, 123(11-12), 2335-2351.
- Davies, H. L., & Smith, I. E. (1974). Tufi-Cape Nelson, Papua New Guinea, Sheets SC/55–8 and SC55-4, Geological Series and Explanatory Notes: Bureau of Mineral Resources, Geology and Geophysics, Department of Minerals and Energy in co-operation with the Geological Survey of Papua New Guinea, scale 1:250,000.
- Davies, H. L. (1978). Folded thrust fault and associated metamorphism in the Suckling-Dayman massif, Papua New Guinea. Geological Survey of Papua New Guinea.
- De Paola, N., Holdsworth, R. E., Viti, C., Collettoni, C., & Bullock, R. (2015). Can grain size sensitive flow lubricate faults during the initial stages of earthquake propagation?. *Earth and Planetary Science Letters*, 431, 48-58.
- Di Toro, G., Han, R., Hirose, T., De Paola, N., Nielsen, S., Mizoguchi, K., ... & Shimamoto, T. (2011). Fault lubrication during earthquakes. *Nature*, 471(7339), 494.
- Dunlop, D. J., & Özdemir, Ö. Rock magnetism//Fundamentals and frontiers, 1997.
- Dunlop, D. J., Özdemir, Ö., & Schmidt, P. W. (1997). Paleomagnetism and paleothermometry of the Sydney Basin 2. Origin of anomalously high unblocking temperatures. *Journal of Geophysical Research: Solid Earth*, 102(B12), 27285-27295.
- Eilon, Z., Abers, G. A., Gaherty, J. B., & Jin, G. (2015). Imaging continental breakup using teleseismic body waves: The Woodlark Rift, Papua New Guinea. *Geochemistry, Geophysics, Geosystems*, 16(8), 2529-2548.
- Elyaszadeh, R., Prior, D. J., Sarkarinejad, K., & Mansouri, H. (2018). Different slip systems controlling crystallographic preferred orientation and intracrystalline deformation of amphibole in mylonites from the Neyriz mantle diapir, Iran. *Journal of Structural Geology*, 107, 38-52.
- Etheridge, M. A., Wall, V. J., Cox, S. F., & Vernon, R. H. (1984). High fluid pressures during regional metamorphism and deformation: implications for mass transport and

- deformation mechanisms. *Journal of Geophysical Research: Solid Earth* (1978–2012), 89(B6), 4344-4358.
- Faulkner, D. R., Mitchell, T. M., Healy, D., & Heap, M. J. (2006). Slip on 'weak' faults by the rotation of regional stress in the fracture damage zone. *Nature*, 444(7121), 922.
- Faulkner, D. R., Mitchell, T. M., Behnsen, J., Hirose, T., & Shimamoto, T. (2011). Stuck in the mud? Earthquake nucleation and propagation through accretionary forearcs. *Geophysical Research Letters*, 38(18).
- Ferris, A., Abers, G. A., Zelt, B., Taylor, B., & Roecker, S. (2006). Crustal structure across the transition from rifting to spreading: the Woodlark rift system of Papua New Guinea. *Geophysical Journal International*, 166(2), 622-634.
- Finlayson, D. M., Drummond, B. J., Collins, C. D. M., & Connelly, J. B. (1977). Crustal structures in the region of the Papuan Ultramafic Belt. *Physics of the Earth and Planetary Interiors*, 14(1), 13-29.
- Getsinger, A. J., Hirth, G., Stünitz, H., & Goergen, E. T. (2013). Influence of water on rheology and strain localization in the lower continental crust. *Geochemistry, Geophysics, Geosystems*, 14(7), 2247-2264.
- Getsinger, A. J., & Hirth, G. (2014). Amphibole fabric formation during diffusion creep and the rheology of shear zones. *Geology*, 42(6), 535-538.
- Gratier, J. P. (2011). Fault permeability and strength evolution related to fracturing and healing episodic processes (years to millennia): the role of pressure solution. *Oil & Gas Science and Technology—Revue d'IFP Energies nouvelles*, 66(3), 491-506.
- Gratier, J. P., Dysthe, D. K., & Renard, F. (2013). The role of pressure solution creep in the ductility of the Earth's upper crust. In *Advances in Geophysics* (Vol. 54, pp. 47-179). Elsevier.
- Han, R., & Hirose, T. (2012). Clay-clast aggregates in fault gouge: An unequivocal indicator of seismic faulting at shallow depths?. *Journal of Structural Geology*, 43, 92-99.
- Hashimoto, M. (1972). Reactions producing actinolite in basic metamorphic rocks. *Lithos*, 5(1), 19-31.
- Healy, D. (2008). Damage patterns, stress rotations and pore fluid pressures in strike-slip fault zones. *Journal of Geophysical Research: Solid Earth*, 113(B12).
- Herwegh, M., Linckens, J., Ebert, A., Berger, A., & Brodhag, S. H. (2011). The role of second phases for controlling microstructural evolution in polymineralic rocks: A review. *Journal of Structural Geology*, 33(12), 1728-1750.
- Hirono, T., Lin, W., Yeh, E. C., Soh, W., Hashimoto, Y., Sone, H., ... & Murayama, M. (2006). High magnetic susceptibility of fault gouge within Taiwan Chelungpu fault: Nondestructive continuous measurements of physical and chemical properties in fault rocks recovered from Hole B, TCDP. *Geophysical Research Letters*, 33(15).
- Hreinsdóttir, S., & Bennett, R. A. (2009). Active aseismic creep on the Alto Tiberina low-angle normal fault, Italy. *Geology*, 37(8), 683-686.

- 1175 Imber, J., Holdsworth, R. E., Butler, C. A., & Strachan, R. A. (2001). A reappraisal of the
1176 Sibson-Scholz fault zone model: The nature of the frictional to viscous (“brittle-ductile”)
1177 transition along a long-lived, crustal-scale fault, Outer Hebrides, Scotland. *Tectonics*,
1178 20(5), 601-624.
- 1179 Imber, J., Holdsworth, R. E., Smith, S. A. F., Jefferies, S. P., & Collettini, C. (2008). Frictional-
1180 viscous flow, seismicity and the geology of weak faults: a review and future directions.
1181 Geological Society, London, Special Publications, 299(1), 151-173.
- 1182 Jackson, J. A. (1987). Active normal faulting and crustal extension. Geological Society, London,
1183 Special Publications, 28(1), 3-17
- 1184 Jackson, J. A., & White, N. J. (1989). Normal faulting in the upper continental crust:
1185 observations from regions of active extension. *Journal of Structural Geology*, 11(1-2), 15-
1186 36.
- 1187 Jefferies, S. P., Holdsworth, R. E., Shimamoto, T., Takagi, H., Lloyd, G. E., & Spiers, C. J.
1188 (2006). Origin and mechanical significance of foliated cataclastic rocks in the cores of
1189 crustal-scale faults: Examples from the Median Tectonic Line, Japan. *Journal of*
1190 *Geophysical Research: Solid Earth*, 111(B12).
- 1191 Kilian, R., Heilbronner, R., & Stünitz, H. (2011). Quartz grain size reduction in a granitoid rock
1192 and the transition from dislocation to diffusion creep. *Journal of Structural Geology*,
1193 33(8), 1265-1284.
- 1194 Lavier, L. L., Roger Buck, W., & Poliakov, A. N. (1999). Self-consistent rolling-hinge model for
1195 the evolution of large-offset low-angle normal faults. *Geology*, 27(12), 1127-1130.
- 1196 Lindley, I. D. (2014). Suckling Dome and the Australian–Woodlark plate boundary in eastern
1197 Papua: the geology of the Keveri and Ada'u Valleys. *Australian Journal of Earth*
1198 *Sciences*, 61(8), 1125-1147.
- 1199 Lister, G. S., & Davis, G. A. (1989). The origin of metamorphic core complexes and detachment
1200 faults formed during Tertiary continental extension in the northern Colorado River
1201 region, USA. *Journal of Structural Geology*, 11(1), 65-94.
- 1202 Little, T. A., Webber, S. M., Mizera, M., Boulton, C., Oesterle, J., Ellis, S., Boles, A., van der
1203 Pluijm, B., Norton, K., Seward, D., Biemiller, J., and Wallace, L. (2019): Evolution of a
1204 rapidly slipping, active low-angle normal fault, Suckling-Dayman Metamorphic Core
1205 Complex, SE Papua New Guinea.
- 1206 Lockner, D. A., Morrow, C., Moore, D., & Hickman, S. (2011). Low strength of deep San
1207 Andreas fault gouge from SAFOD core. *Nature*, 472(7341), 82.
- 1208 Mainprice, D., Bachmann, F., Hielscher, R., & Schaeben, H. (2015). Descriptive tools for the
1209 analysis of texture projects with large datasets using MTEX: strength, symmetry and
1210 components. Geological Society, London, Special Publications, 409(1), 251-271.
- 1211 Menegon, L., Fousseis, F., Stünitz, H., & Xiao, X. (2015). Creep cavitation bands control porosity
1212 and fluid flow in lower crustal shear zones. *Geology*, 43(3), 227-230.
- 1213 Mishima, T., Hirano, T., Soh, W., & Song, S. R. (2006). Thermal history estimation of the
1214 Taiwan Chelungpu fault using rock-magnetic methods. *Geophysical research letters*,
1215 33(23).

- Mishima, T., Hirano, T., Nakamura, N., Tanikawa, W., Soh, W., & Song, S. R. (2009). Changes to magnetic minerals caused by frictional heating during the 1999 Taiwan Chi-Chi earthquake. *Earth, planets and space*, 61(6), 797-801.
- Mizera, M. (2019). Deformational Processes Accommodating Slip on an Active Low-Angle Normal Fault, Suckling-Dayman Metamorphic Core Complex, Papua New Guinea.
- Mizera, M., Little, T. A., Biemiller, J., Ellis, S., Webber, S., & Norton, K. P. (2019). Structural and Geomorphic Evidence for Rolling-Hinge Style Deformation of an Active Continental Low-Angle Normal Fault, SE Papua New Guinea. *Tectonics*, 38(5), 1556-1583.
- Montési, L. G. (2013). Fabric development as the key for forming ductile shear zones and enabling plate tectonics. *Journal of Structural Geology*, 50, 254-266.
- Moore, D. E., & Lockner, D. A. (2004). Crystallographic controls on the frictional behavior of dry and water-saturated sheet structure minerals. *Journal of Geophysical Research: Solid Earth*, 109(B3).
- Moore, D. E., & Rymer, M. J. (2012). Correlation of clayey gouge in a surface exposure of serpentinite in the San Andreas Fault with gouge from the San Andreas Fault Observatory at Depth (SAFOD). *Journal of Structural Geology*, 38, 51-60.
- Moore, D. E. (2014). Comparative mineral chemistry and textures of SAFOD fault gouge and damage-zone rocks. *Journal of Structural Geology*, 68, 82-96.
- Moore, D. E., Lockner, D. A., & Hickman, S. (2016). Hydrothermal frictional strengths of rock and mineral samples relevant to the creeping section of the San Andreas Fault. *Journal of Structural Geology*, 89, 153-167.
- Niemeijer, A. R., & Spiers, C. J. (2005). Influence of phyllosilicates on fault strength in the brittle-ductile transition: Insights from rock analogue experiments. *Geological Society, London, Special Publications*, 245(1), 303-327.
- Offerhaus, L. J., Wirth, R., & Dresen, G. (2001). High-temperature creep of polycrystalline albite. *Deformation Mechanisms, Rheology and Tectonics*, 124, 107-131.
- Oohashi, K., Hirose, T., & Shimamoto, T. (2011). Shear-induced graphitization of carbonaceous materials during seismic fault motion: Experiments and possible implications for fault mechanics. *Journal of Structural Geology*, 33(6), 1122-1134.
- Österle, J. (2019). The thermo-tectonic evolution of the Suckling-Dayman metamorphic core complex, southeastern Papua New Guinea (Doctoral dissertation, Victoria University of Wellington).
- Österle, J. E., Stockli, D. F., Seward, D., & Little, T. A. Dating of young (< 1 Ma) tephras: Using U-Pb (zircon) and (U-Th [-Sm])/He (zircon, apatite, magnetite) chronometers to unravel the eruption age of a tephra in the Woodlark Rift of Papua New Guinea. *Terra Nova*.
- Özdemir, Ö., & Banerjee, S. K. (1984). High temperature stability of maghemite (γ -Fe₂O₃). *Geophysical research letters*, 11(3), 161-164.
- Özdemir, Ö. (1990). High-temperature hysteresis and thermoremanence of single-domain maghemite. *Physics of the Earth and planetary interiors*, 65(1-2), 125-136.

- 1255 Pearce, M. A., Wheeler, J., & Prior, D. J. (2011). Relative strength of mafic and felsic rocks
1256 during amphibolite facies metamorphism and deformation. *Journal of Structural Geology*,
1257 33(4), 662-675.
- 1258 Platt, J. P. (2015). Rheology of two-phase systems: A microphysical and observational approach.
1259 *Journal of Structural Geology*, 77, 213-227.
- 1260 Platt, J. P., Behr, W. M., & Cooper, F. J. (2015). Metamorphic core complexes: windows into the
1261 mechanics and rheology of the crust. *Journal of the Geological Society*, 172(1), 9-27.
- 1262 Rempe, M., Smith, S. A., Ferri, F., Mitchell, T. M., & Di Toro, G. (2014). Clast-cortex
1263 aggregates in experimental and natural calcite-bearing fault zones. *Journal of Structural*
1264 *Geology*, 68, 142-157.
- 1265 Rice, J. R. (1992). Fault stress states, pore pressure distributions, and the weakness of the San
1266 Andreas fault. *International Geophysics*, 51, 475-503.
- 1267 Richard, J., Gratier, J. P., Doan, M. L., Boullier, A. M., & Renard, F. (2014). Rock and mineral
1268 transformations in a fault zone leading to permanent creep: Interactions between brittle
1269 and viscous mechanisms in the San Andreas Fault. *Journal of Geophysical Research:*
1270 *Solid Earth*, 119(11), 8132-8153.
- 1271 Rigo, A., Lyon-Caen, H., Armijo, R., Deschamps, A., Hatzfeld, D., Makropoulos, K., ... &
1272 Kassaras, I. (1996). A microseismic study in the western part of the Gulf of Corinth
1273 (Greece): implications for large-scale normal faulting mechanisms. *Geophysical Journal*
1274 *International*, 126(3), 663-688.
- 1275 Robinson, D., Schmidt, S. T., & De Zamora, A. S. (2002). Reaction pathways and reaction
1276 progress for the smectite-to-chlorite transformation: evidence from hydrothermally
1277 altered metabasites. *Journal of metamorphic Geology*, 20(1), 167-174.
- 1278 Rowe, C. D., Meneghini, F., & Moore, J. C. (2011). Textural record of the seismic cycle: Strain-
1279 rate variation in an ancient subduction thrust. *Geological Society, London, Special*
1280 *Publications*, 359(1), 77-95.
- 1281 Rowe, C. D., & Griffith, W. A. (2015). Do faults preserve a record of seismic slip: A second
1282 opinion. *Journal of Structural Geology*, 78, 1-26.
- 1283 Rutter, E. H., & Mainprice, D. H. (1979). On the possibility of slow fault slip controlled by a
1284 diffusive mass transfer process. *Gerlands Beitrage zur Geophysik*, 88(2), 154-162.
- 1285 Rutter, E. H. (1983). Pressure solution in nature, theory and experiment. *Journal of the*
1286 *Geological Society*, 140(5), 725-740.
- 1287 Sammis, C. G., & Ben-Zion, Y. (2008). Mechanics of grain-size reduction in fault zones. *Journal*
1288 *of Geophysical Research: Solid Earth*, 113(B2).
- 1289 Scholz, C. H. (2002). *The Mechanics of Earthquakes and Faulting*. Cambridge University Press,
1290 Cambridge, 471 p.
- 1291 Sibson, R. H. (1985). A note on fault reactivation. *Journal of Structural Geology*, 7(6), 751-754.
- 1292 Sibson, R. H. (1992). Implications of fault-valve behaviour for rupture nucleation and
1293 recurrence. *Tectonophysics*, 211(1-4), 283-293.

- 1294 Skelton, A. D. L., Valley, J. W., Graham, C. M., Bickle, M. J., & Fallick, A. E. (2000). The
1295 correlation of reaction and isotope fronts and the mechanism of metamorphic fluid flow.
1296 Contributions to Mineralogy and Petrology, 138(4), 364-375.
- 1297 Skemer, P., Katayama, I., Jiang, Z., & Karato, S. I. (2005). The misorientation index:
1298 Development of a new method for calculating the strength of lattice-preferred orientation.
1299 Tectonophysics, 411(1-4), 157-167.
- 1300 Sleep, N. H., & Blanpied, M. L. (1992). Creep, compaction and the weak rheology of major
1301 faults. Nature, 359(6397), 687-692.
- 1302 Smith, I. E. & Davies, H. L. (1976). Geology of the Southeast Papuan Mainland. Bureau of
1303 mineral resources, geology and geophysics, Bulletin 165.
- 1304 Smith, S. A. F., Holdsworth, R. E., Collettini, C., & Pearce, M. A. (2011). The microstructural
1305 character and mechanical significance of fault rocks associated with a continental low-
1306 angle normal fault: the Zuccale Fault, Elba Island, Italy. Geological Society, London,
1307 Special Publications, 359(1), 97-113.
- 1308 Smith, I. E. (2013). The chemical characterization and tectonic significance of ophiolite terrains
1309 in southeastern Papua New Guinea. Tectonics, 32(2), 159-170.
- 1310 Smith, S. A. F., Di Toro, G., Kim, S., Ree, J. H., Nielsen, S., Billi, A., & Spiess, R. (2013).
1311 Coseismic recrystallization during shallow earthquake slip. Geology, 41(1), 63-66.
- 1312 Speckbacher, R., Behrmann, J. H., Nagel, T. J., Stipp, M., & Mahlke, J. (2012). Fluid flow and
1313 metasomatic fault weakening in the Moresby Seamount detachment, Woodlark Basin,
1314 offshore Papua New Guinea. Geochemistry, Geophysics, Geosystems, 13(11).
- 1315 Speckbacher, R., Stipp, M., Behrmann, J. H., & Heidelbach, F. (2013). Fluid-assisted fracturing,
1316 cataclasis, and resulting plastic flow in mylonites from the Moresby Seamount
1317 detachment, Woodlark Basin. Journal of Structural Geology, 56, 156-171.
- 1318 Spencer, J. E. (1984). Role of tectonic denudation in warping and uplift of low-angle normal
1319 faults. Geology, 12(2), 95-98.
- 1320 Spencer, J. E., & Chase, C. G. (1989). Role of crustal flexure in initiation of low-angle normal
1321 faults and implications for structural evolution of the Basin and Range province. Journal
1322 of Geophysical Research: Solid Earth, 94(B2), 1765-1775.
- 1323 Spencer, J. E. (2010). Structural analysis of three extensional detachment faults with data from
1324 the 2000 Space-Shuttle Radar Topography Mission. GSA Today, 20(8), 4-10.
- 1325 Stenvall, C. A., Fagereng, Å., & Diener, J. F. (2019). Weaker than weakest: on the strength of
1326 shear zones. Geophysical Research Letters, 46(13), 7404-7413.
- 1327 Stewart, M., Holdsworth, R. E., & Strachan, R. A. (2000). Deformation processes and weakening
1328 mechanisms within the frictional–viscous transition zone of major crustal-scale faults:
1329 insights from the Great Glen Fault Zone, Scotland. Journal of Structural Geology, 22(5),
1330 543-560.
- 1331 Stipp, M., Stünitz, H., Heilbronner, R., & Schmid, S. M. (2002). Dynamic recrystallization of
1332 quartz: correlation between natural and experimental conditions. Geological Society,
1333 London, Special Publications, 200(1), 171-190.

- Stipp, M., & Kunze, K. (2008). Dynamic recrystallization near the brittle-plastic transition in naturally and experimentally deformed quartz aggregates. *Tectonophysics*, 448(1-4), 77-97.
- Stünitz, H., & Tullis, J. (2001). Weakening and strain localization produced by syn-deformational reaction of plagioclase. *International Journal of Earth Sciences*, 90(1), 136-148.
- Surace, I. R., Clauer, N., Th  lin, P., & Pfeifer, H. R. (2011). Structural analysis, clay mineralogy and K–Ar dating of fault gouges from Centovalli Line (Central Alps) for reconstruction of their recent activity. *Tectonophysics*, 510(1-2), 80-93.
- Tanikawa, W., Mishima, T., Hirono, T., Lin, W., Shimamoto, T., Soh, W., & Song, S. R. (2007). High magnetic susceptibility produced in high-velocity frictional tests on core samples from the Chelungpu fault in Taiwan. *Geophysical Research Letters*, 34(15).
- Tanikawa, W., Mishima, T., Hirono, T., Soh, W., & Song, S. R. (2008). High magnetic susceptibility produced by thermal decomposition of core samples from the Chelungpu fault in Taiwan. *Earth and Planetary Science Letters*, 272(1-2), 372-381.
- Taylor, B., & Huchon, P. (2002). Active continental extension in the western Woodlark Basin: a synthesis of Leg 180 results. In *Proceedings of the Ocean Drilling Program, Scientific Results* (Vol. 180, pp. 1-36). P. Huchon, B. Taylor, and A. Klaus.
- Tregoning, P., Lambeck, K., Stolz, A., Morgan, P., McClusky, S. C., Beek, P., ... & Murphy, B. (1998). Estimation of current plate motions in Papua New Guinea from Global Positioning System observations. *Journal of Geophysical Research: Solid Earth*, 103(B6), 12181-12203.
- Vadacca, L., Casarotti, E., Chiaraluce, L., & Cocco, M. (2016). On the mechanical behaviour of a low-angle normal fault: the Alto Tiberina fault (Northern Apennines, Italy) system case study. *Solid Earth*, 7(6), 1537-1549.
- Verberne, B. A., Pl  mper, O., de Winter, D. M., & Spiers, C. J. (2014). Superplastic nanofibrous slip zones control seismogenic fault friction. *Science*, 346(6215), 1342-1344.
- Verberne, B. A., Niemeijer, A. R., De Bresser, J. H., & Spiers, C. J. (2015). Mechanical behavior and microstructure of simulated calcite fault gouge sheared at 20–600 C: Implications for natural faults in limestones. *Journal of Geophysical Research: Solid Earth*, 120(12), 8169-8196.
- Viegas, G., Menegon, L., & Archanjo, C. (2016). Brittle grain-size reduction of feldspar, phase mixing and strain localization in granitoids at mid-crustal conditions (Pernambuco shear zone, NE Brazil). *Solid Earth*, 7(2), 375-396.
- Wallace, L. M., Stevens, C., Silver, E., McCaffrey, R., Loratung, W., Hasiata, S., ... & Taugaloidi, J. (2004). GPS and seismological constraints on active tectonics and arc-continent collision in Papua New Guinea: Implications for mechanics of microplate rotations in a plate boundary zone. *Journal of Geophysical Research: Solid Earth*, 109(B5).

- Wallace, L. M., Ellis, S., Little, T., Tregoning, P., Palmer, N., Rosa, R., ... & Kwazi, J. (2014). Continental breakup and UHP rock exhumation in action: GPS results from the Woodlark Rift, Papua New Guinea. *Geochemistry, Geophysics, Geosystems*, 15(11), 4267-4290.
- Watson, E. (2019). Using paleomagnetism to test rolling hinge behaviour of an active low angle normal fault, Papua New Guinea.
- Warren, J. M., & Hirth, G. (2006). Grain size sensitive deformation mechanisms in naturally deformed peridotites. *Earth and Planetary Science Letters*, 248(1-2), 438-450.
- Webb, L. E., Baldwin, S. L., Little, T. A., & Fitzgerald, P. G. (2008). Can microplate rotation drive subduction inversion?. *Geology*, 36(10), 823-826.
- Webber, S., Norton, K. P., Little, T. A., Wallace, L. M., & Ellis, S. (2018). How fast can low-angle normal faults slip? Insights from cosmogenic exposure dating of the active Mai'iu fault, Papua New Guinea. *Geology*, 46(3), 227-230.
- Webber, S., Little, T. A., Norton, K. P., Österle, J., Mizera, M., Seward, D., & Holden, G. (2020). Progressive back-warping of a rider block atop an actively exhuming, continental low-angle normal fault. *Journal of Structural Geology*, 130, 103906.
- Westaway, R. (2005). Active low-angle normal faulting in the Woodlark extensional province, Papua New Guinea: A physical model. *Tectonics*, 24(6).
- Whitney, D. L., Teyssier, C., Rey, P., & Buck, W. R. (2013). Continental and oceanic core complexes. *Geological Society of America Bulletin*, 125(3-4), 273-298.
- Wintsch, R. P., Christoffersen, R., & Kronenberg, A. K. (1995). Fluid-rock reaction weakening of fault zones. *Journal of Geophysical Research: Solid Earth*, 100(B7), 13021-13032.
- Wintsch, R. P., & Yeh, M. W. (2013). Oscillating brittle and viscous behavior through the earthquake cycle in the Red River Shear Zone: Monitoring flips between reaction and textural softening and hardening. *Tectonophysics*, 587, 46-62.
- Yang, T., Chen, J., Wang, H., & Jin, H. (2012). Rock magnetic properties of fault rocks from the rupture of the 2008 Wenchuan earthquake, China and their implications: Preliminary results from the Zhaojiagou outcrop, Beichuan County (Sichuan). *Tectonophysics*, 530, 331-341.
- Yavuz, F., Kumral, M., Karakaya, N., Karakaya, M. Ç., & Yıldırım, D. K. (2015). A Windows program for chlorite calculation and classification. *Computers & Geosciences*, 81, 101-113.
- Yin, A. (1989). Origin of regional, rooted low-angle normal faults: A mechanical model and its tectonic implications. *Tectonics*, 8(3), 469-482.